PHILOSOPHICAL TRANSACTIONS A

royalsocietypublishing.org/journal/rsta

Review

Cite this article: Yaxin Z, Hongxin Z, Wei K, Lan W, Mittleman DM, Ziqiang Y. 2020 Terahertz smart dynamic and active functional electromagnetic metasurfaces and their applications. *Phil. Trans. R. Soc. A* **378**: 20190609.
http://dx.doi.org/10.1098/rsta.2019.0609

Accepted: 7 July 2020

One contribution of 15 to a theme issue 'Advanced electromagnetic non-destructive evaluation and smart monitoring'.

Subject Areas:
electromagnetism, optics, materials science

Keywords:
metasurfaces, terahertz, coding, programmable, tunable

Author for correspondence:
Yang Ziqiang
e-mail: yangziqiang@uestc.edu.cn

†These are co-first authors.

THE ROYAL SOCIETY PUBLISHING

Terahertz smart dynamic and active functional electromagnetic metasurfaces and their applications

Zhang Yaxin[1,†], Zeng Hongxin[1,†], Kou Wei[1], Wang Lan[1], Daniel M. Mittleman[2] and Yang Ziqiang[1]

[1]Terahertz Science Cooperative Innovation Center, University of Electronic Science and Technology of China, Chengdu 610054, People's Republic of China
[2]School of Engineering, Brown University, Providence, RI 02912, USA

ZY, 0000-0002-2265-3614; ZH, 0000-0002-4404-9485

The demand for smart and multi-functional applications in the terahertz (THz) frequency band, such as for communication, imaging, spectroscopy, sensing and THz integrated circuits, motivates the development of novel active, controllable and informational devices for manipulating and controlling THz waves. Metasurfaces are planar artificial structures composed of thousands of unit cells or metallic structures, whose size is either comparable to or smaller than the wavelength of the illuminated wave, which can efficiently interact with the THz wave and exhibit additional degrees of freedom to modulate the THz wave. In the past decades, active metasurfaces have been developed by combining diode arrays, two-dimensional active materials, two-dimensional electron gases, phase transition material films and other such elements, which can overcome the limitations of conventional bulk materials and structures for applications in compact THz multi-functional antennas, diffractive devices, high-speed data transmission and high-resolution imaging. In this paper, we provide a brief overview of the development of dynamic and active functional electromagnetic metasurfaces and their applications in the THz band in recent years. Different kinds of active metasurfaces are cited and introduced. We believe that, in the future, active metasurfaces will be combined with digitalization and coding to yield more intelligent metasurfaces, which can be used to realize smart THz wave beam scanning, automatic

target recognition imaging, self-adaptive directional high-speed data transmission network, biological intelligent detection and other such applications.

This article is part of the theme issue 'Advanced electromagnetic non-destructive evaluation and smart monitoring'.

1. Introduction

With the rapid development of metamaterials, researchers worldwide have extensively focused on the associated research direction since the start of this century [1–4]. Metamaterials are artificial structures composed of an array of designed and periodically arranged individual units, which can exhibit specific electromagnetic properties [5–9]. In the microwave band, metamaterials can be developed by using a three-dimensional (3D) arbitrarily arranged array to exhibit various characteristics such as those related to cloaking, abnormal Cherenkov radiation, Doppler effect and negative index of refraction.

Since the turn of the century, it has been known that terahertz (THz) technology, which is a relatively novel research area, can be applied to imaging, spectroscopy and communication applications. Compared with microwaves, THz waves have higher frequency and bandwidth to carry more information. Therefore, they have great potential for application in medium–short distance and large-capacity wireless communication. THz waves also have a higher spatial resolution, and their imaging has a greater depth of field while maintaining the same spatial resolution. In addition, many organic molecules have strong absorption and dispersion characteristics in the THz band. The THz spectrum of substances contains rich physical and chemical information, which gives them unique features similar to fingerprints. Therefore, the THz spectrum detection technology cannot only distinguish the shape of the object but also identify the composition of the object. Numerous unique advantages of THz waves promote the demand for high-performance THz devices. In the past, 3D metamaterials have been a useful way to design THz devices. However, with the increase in the working frequency, processing the 3D structure in a feasible manner becomes challenging. Recently, 2D metamaterials known as metasurfaces, which exhibit a higher flexibility, more intelligent characteristics, appropriate design characteristics and suitability for higher frequency band applications, have been extensively considered by the scientific community [10–14]. Because of its low profile and compactness, metasurfaces can be implemented through standard microprocessing techniques and integrated easily and efficiently into THz systems. Therefore, metasurfaces are of great significance for the development of highly integrated and efficient THz devices. In particular, such metasurfaces have been used to achieve THz modulators, antennas, polarization converters, filters and planar lens with designed and fixed metallic structure arrays.

Initially, THz metasurfaces were developed, whose functions are determined during the manufacturing process, called passive metasurfaces. In 2011, Yu and Capasso's team proposed abrupt phase gradient metasurfaces to realize anomalous reflection and refraction, by extending the traditional Snell's Law to a generalized Snell's Law [15]. Recently, by implementing the abrupt phase and amplitude response on metasurfaces, various functional devices have been designed and reported. An excellent example of the idea of gradient metasurfaces is a metalens, a plane lens in which electromagnetic waves are injected into the lens in parallel, and the propagation path is changed using the metasurface with a specific phase gradient at the surface. In 2018, Liang *et al.* [16] proposed an ultrathin THz metasurface integrated with a lens for polarization division multiplexing, in which the focus of two orthogonally polarized THz waves can be independently controlled. In addition to focusing function, a THz polarization beam splitting device can be designed by applying metasurface. In 2019, Zeng *et al*. [17] proposed an electromagnetic anisotropic gradient metasurface to achieve the effect of polarized beam separation. It demonstrates the metasurface effectively split the normal and incident x- and y-polarized components at 0.32–0.42 THz in different planes. There are also

various reports on functions including the metasurface lens [16,18–26], vortex beam generators [27–36] and polarization beam splitters [37–43]. The phase of metallic structures on the gradient metasurface maintains a certain special relationship, which provides powerful electromagnetic wave manipulation capabilities. To further explore the deeper internal association between the various phase distributions and electromagnetic waves, in 2014, Cui's research group proposed the concept of coding metamaterials and coding metasurfaces [44]. Coding metasurfaces provide more freedom and capabilities for manipulating electromagnetic waves through digital characterization. Researchers do not need to consider the specific metallic structures constituting the ultimate coding metasurface, because the coding patterns determine the far-field and near-field scattering fields, and the distribution of these metallic structures in the metasurface can be clarified. Following this concept of coding metasurfaces, different functions passive metasurfaces and methods have been proposed and presented, such as reducing radar cross-section [45–50], directional deflection of THz beams [17,51–54], hologram imaging [55–63] and so on. However, in applications requiring THz wave variation, passive metasurfaces cannot perform the required functions, such as high-speed modulated metasurfaces for THz communication, wavefront reconstructed metasurfaces for THz imaging, beam scanning in THz radar and so on. To develop more flexible and manoeuvrable devices for real-time THz application systems such as spectroscopy applications, imaging, beam scanning and high-speed communication, the demand for smart, integrated and multi-functional devices has increased [64].

To change or reconstruct the characteristics of passive metasurfaces, the metasurfaces need to be redesigned and reprepared. The demand of smart devices led to the development of active metasurfaces. In addition, with the cross-investigation of artificial microstructures in different disciplines, active metasurfaces composed of metallic microstructure and tunable components gradually developed, yielding a new approach to developing active THz smart functional devices. By controlling the electrical characteristics or material properties of the tunable components through external voltage, light or temperature, the resonant properties of the metasurfaces can be reconfigured, thereby realizing the control of the incident THz waves. Generally, response speed and depth are the critical performance indexes for active metasurfaces. Therefore, many outstanding studies focus on improving response speed and depth. In the past 10 years, the performance of THz active metasurface has developed rapidly, response depth increased from about 40% to nearly 100%, and response speed increased thousands of times from kHz (figure 1). One important early example is the work of Chen *et al*. [65] from Los Alamos National Lab, who combined a metasurface with a hybrid semiconductor to realize a tunable artificial microstructure that can modulate the amplitude and phase of THz waves. Subsequently, different mechanisms, materials and geometric constructs were proposed and implemented to realize different functional devices in the THz band [17,24,66–72]. Thus, in the past decade, an increasing number of outstanding achievements have been reported. These innovations include phase shifters, all-optical switches, modulators, wavefront shapers, memory devices and beam scanners, and are enabled by integration with doped silicon, two-dimensional electron gas (2DEG) materials, phase change materials, superconducting materials and other such materials. In addition, by applying digital circuits and a dynamic metasurface, Cui's group reported on programmable active metasurfaces in 2014 [44], which were further evolved into information metamaterials and metasurfaces in 2016. In this concept, digital information technology and active metasurfaces are combined to construct a smart device that can be used to realize real-time manipulation of THz wave and multi-functional characteristics. Compared to conventional metasurfaces, programmable active metasurfaces consist of tunable components controlled by an FPGA (field-programmable gate array). FPGA adopts the concept of logic cell array, which includes configurable logic modules, input and output modules and internal wiring. It can store programming information for different functions of the active metasurface. The bias voltage of the tunable components is connected to the FPGA to permit real-time wave-based information processing to the physical levels of the metasurfaces. By using the FPGA and integrated digital circuits, an information metasurface can realize wavefront coding, beam alignment, information transfer and environmental sensor functions simultaneously. Such a creative concept builds

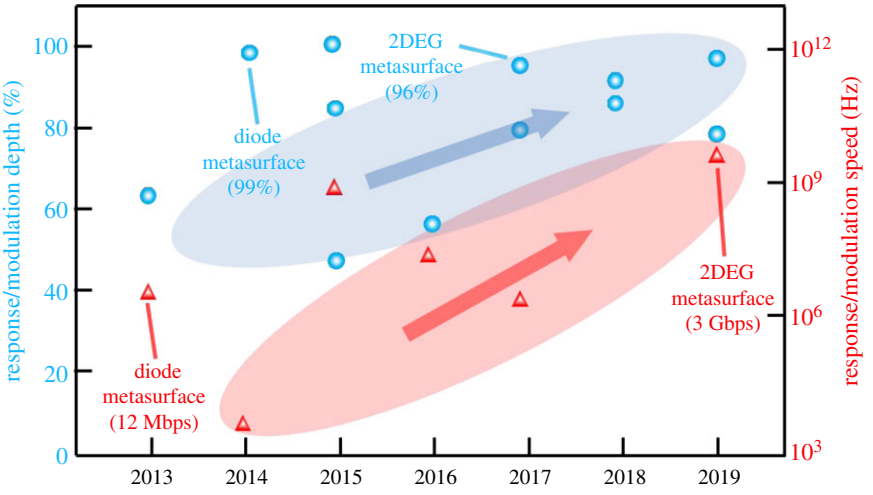

Figure 1. Progress of THz active metasurfaces. (Online version in colour.)

a bridge between digital information system and physical surface, which could lead to a revolutionary development of multi-functional THz information systems. Recent works have demonstrated that the active metasurface can be adapted to different kinds of application systems including holograms, imaging systems and communication systems.

Considering the previous outstanding achievements pertaining to active metasurfaces and their applications, this paper reviews the studies from 2015 to now concerning the active metasurfaces to realize the manipulation of THz waves, high-speed wireless communication, imaging application system, introduce the operation principles and mechanisms of various active functional metasurfaces and outline predictions for future research directions of sensing and monitoring. The remaining paper is organized as follows: §2 reviews the research progress of THz active metasurfaces with different active components, mainly focusing on diode metasurfaces, 2DEG metasurfaces and 2D material metasurfaces. Section 3 highlights the recent application of metasurfaces in high-speed data communication, imaging and biological detection as well as the prospect of THz active metasurfaces for future applications.

2. Terahertz active metasurface

Tunable components are the most critical factors to the THz active metasurface. Therefore, in this section, several types of metasurfaces composed of different tunable components will be illustrated and compared from the principles to the characteristics. This section is structured in three subsections attending to the main THz metasurface: diode THz metasurfaces, 2DEG THz metasurfaces, and 2D material and phase transition material film THz metasurface. Some of the representative results of THz active metasurfaces integrating different tunable components are shown in table 1. The conventional GaAs Schottky diode metasurfaces are comfortable to be manufactured and implemented with an external electrical field; the 2DEG metasurfaces have high response speed and deep response amplitude depth; the 2D graphene materials metasurfaces have great potentials in the ultrafast switch; the phase transition materials metasurfaces could realize the temperature sensing electromagnetic response. Various tunable components have their own distinctive characteristics, opening new opportunities for the THz metasurface to be smart.

(a) Diode metasurface

As one of the most recognizable core elements for electrical control, diodes have been applied in several research areas. Specifically, varactor and rheostatic diodes are used in various systems. It is

Table 1. Basic performances of THz active metasurfaces with different tunable components.

tunable components	response speed or time	response amplitude depth (%)	response phase shift	reference
Schottky diode	12 MHz	62	—	2013 [73]
Schottky diode	1 KHz	99	—	2014 [74]
Schottky diode	—	46	—	2015 [75]
2DEG	1 GHz	85	1.19 rad	2015 [69]
2DEG	2.7 MHz	80	0.67 rad	2017 [76]
2DEG	—	90	2.27 rad	2018 [77]
2DEG	—	96	—	2017 [78]
2DEG	48 MHz	45	—	2016 [79]
2DEG	3 GHz	93	—	2019 [80]
Graphene	100 fs	35	—	2019 [81]
Graphene	19 μs	72	—	2019 [82]
VO_2	—	27	—	2018 [83]
VO_2	—	92	2.4 rad	2018 [70]
VO_2	—	95	—	2019 [84]
liquid crystal	50 ms	100	—	2015 [85]

well known that by loading an external voltage, the capacitance, resistance, carrier concentration and depletion characteristics of the diodes can be tuned. Thus, in as early as 2006, a combination of semiconductors and metasurfaces to achieve real-time control of electromagnetic waves in the THz band was proposed [65]. By using the Schottky diode effect of the doped metal–semiconductor, the metasurface can control the amplitude of electromagnetic waves. In these cases, the injection and depletion of the carriers of the diode metasurfaces are controlled by changing the gate voltage. Along with this concept, THz diode metasurfaces with different structures have been developed. In 2013, Padilla *et al.* [73] implemented a THz diode metasurface through a reflective metasurface combined with a Schottky structure, as shown in figure 2*a*. The metasurface consists of two metal layers with a medium in between. The top layer is constructed to respond to the electronic components of the incoming THz wave. The bottom ground plane layer is relatively close to the top layer, thus coupling the external magnetic field. In this case, the frequency of the resonant absorption can be adjusted by changing the carrier concentration between the surface metal and semiconductor substrate by applying a reverse voltage bias. The average modulation depth of the entire array is 62%, and the rate is 12 MHz. This THz diode metasurface has been applied for THz compressive imaging [86,87]. To further increase the modulation depth, in 2014, Mittleman *et al.* [74] combined the Schottky gate structure to design a switchable diffraction grating mechanism, in which alternating columns are composed of split-ring resonators with amplitude and phase modulation at different bias voltages, as shown in figure 2*b*. The maximum transmittance in the two adjacent columns, the structure exhibits the strongest diffraction at a resonance frequency of 400 GHz. This structure exhibits broadband characteristics at a diffraction angle of 36.1° and achieves a modulation depth of up to 22 dB. Moreover, the team proposed the THz ellipsometry mechanism and predicted that guided wave structures with substantial phase modulation could be realized [88]. Experimental results indicated that this structure can realize a phase modulation of 0.4 rad mm^{-1} at 300 GHz. This work enhances the modulation depth of the THz wave amplitude by the metasurface through the principle of grating diffraction, but its modulation bandwidth is limited. To improve the modulation bandwidth, in 2015, by combining the C-shape split resonant ring (SRR) diode

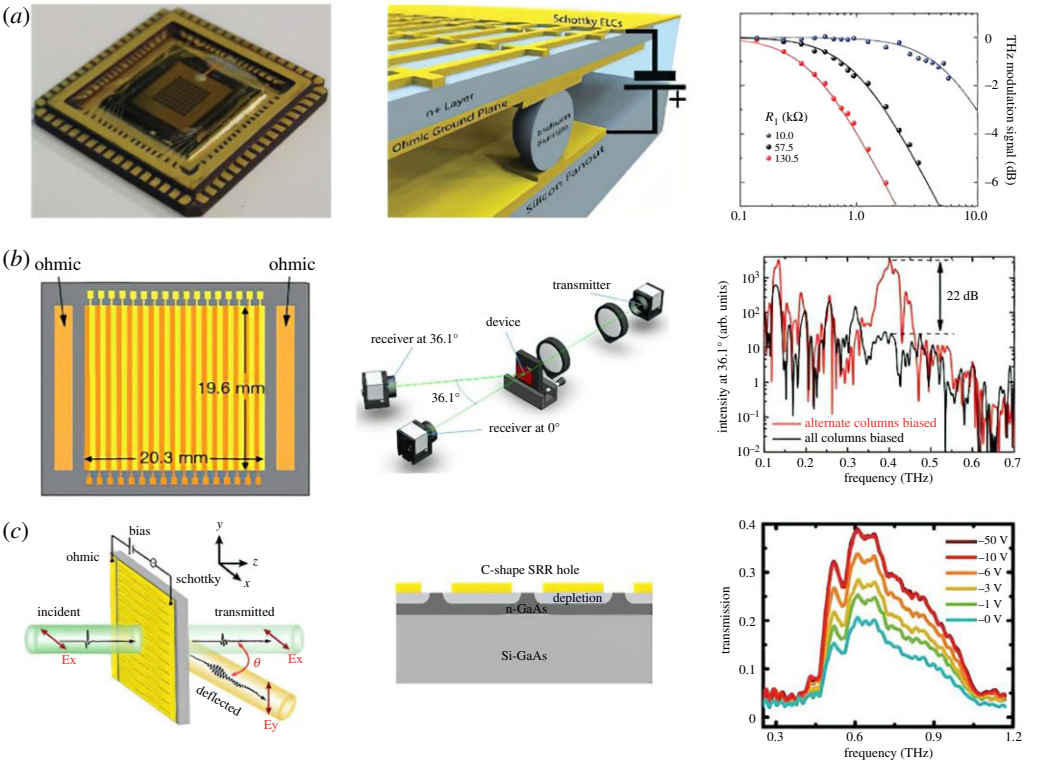

Figure 2. (*a*) Switchable THz spatial light-active metasurface based on the Schottky structure, and its schematic. The figure on the right shows the modulation rate obtained by measuring the RC time constant according to the external series resistance [73]. (*b*) Metasurface grating based on the Schottky structure and experimental structure for THz transmission measurement. The figure on the right shows the intensity curve under different biases when the diffraction angle is 36.1° [74]. (*c*) Complementary THz metasurface structure based on the diode effect, and transmission spectrum of the deflected wave [75]. (Online version in colour.)

metasurface, Su *et al.* designed a THz phase discontinuously active metasurface, as shown in figure 2*c* [75]. By applying the external bias voltage, the metasurface could achieve a wide-band frequency response ranging from 0.48 to 0.93 THz in a wide-angle range of 26°–81° with 46% modulation depth. As the earliest THz active metasurface, diode metasurfaces have been used to realize the effective manipulation of THz waves, but its modulation depth and modulation rate need to be further improved.

(b) Two-dimensional electron gases metasurface

As the earliest THz active metasurface, diode metasurfaces have been used to realize the effective manipulation of THz waves, as mentioned previously. In recent years, with the development of tunable heterostructures, 2DEG have been used for developing different kinds of THz devices such as THz amplifiers, detectors, switches and modulators. The 2DEG is usually induced by spontaneous polarization and piezoelectric polarization in the heterostructure. By applying the 2DEG, high electron mobility transistors (HEMT) have been developed and used in many electronic devices. Due to its high mobility and carrier concentration, 2DEG exhibits potential for developing active dynamic composite metasurfaces with grid controlling external circuits. By controlling the electronic transport properties of the 2DEG, the distribution of the electrons and free-transport carriers can be manipulated. In general, the nano-structured 2DEG components are embedded within the metallic structures to construct an active metasurface based on the

composite HEMT array, and thus, this configuration is known as a 2DEG metasurface. The metallic metasurface acts not only as an electromagnetic resonator but also as part of the composite HEMTs. Usually, the metallic artificial microstructures are placed in contact with the 2DEG to construct the source and drain electrodes, while a controlling grid is connected with the centre to ensure that the external signal voltage can be loaded on the 2DEG. The basic mechanism contains two phases: first, no voltage exists; the drain and source metallic electrodes are connected, and the incident THz wave can induce an initial resonance. When a bias is applied between two electrodes, the electrons in the epitaxial doped layer are depleted, and the free-transport carriers disappear. Furthermore, the drain and source electrodes are disconnected, which reconfigures the metasurface such that another resonance can be induced. Thus, during the external voltage control process, a significant mode conversion occurs in the metasurface, thereby enhancing the amplitude or phase modulation of the transmitted and reflected THz waves.

Such an active THz 2DEG metasurface was first proposed by Padilla's group in 2011 [89]. In this work, the metasurface and transistor model were fabricated on the GaAs substrate, and monolithic integration of the lnGaAs/GaAs HEMT into each metallic structure was performed. Resonant mode switching could be achieved by changing the connected state at the channel by changing the voltage. The active metasurface could realize a high-speed modulation of 10 MHz for THz waves with a modulation depth of 30%. Although this design concept is of great significance for THz high-speed modulation, its modulation rate and modulation depth need to be further improved. Along with the concept of 2DEG metasurface, in 2015, considering the excellent characteristics of high 2DEG concentration and mobility, the InAlN/AlN/GaN/AlN/GaN double-channel heterostructure was combined with an I-shaped metallic structure [69], as shown in figure 3*a*. A resonance conversion between two different dipole resonances was achieved by applying an external voltage, which can realize an effective modulation of the amplitude of the transmitted THz wave. The results demonstrated that a modulation depth of 85%, monophonic modulation speed of 1 GHz, eye pattern data transmission rate of 0.2 Gbps and phase shift of 1.19 rad could be achieved, thereby indicating that the 2DEG metasurface can be used to realize high-performance THz dynamic devices. Subsequently, Zhang used a single-channel AlGaN/GaN heterostructure for THz wave modulation [67]. Since the conductance in a single-channel heterostructure is lower than that in a dual-channel heterostructure, the modulation depth at 0.86 THz is 33%, and the modulation speed is 20 MHz. To improve the performance of the active metasurface, Huang *et al*. [90] proposed a plasma THz active metasurface developed by coupling the periodic grating metasurface with 2DEG. Tunable 2D plasmonic cavities are formed by the voltage applied to the grating, thereby controlling the resonance state of the 2D plasmons and achieving a modulation depth of 93% and a 3 dB bandwidth of 400 kHz. To further improve the performance of 2DEG-based THz devices, in 2019, an active collective-individual state conversion mechanism with a staggered netlike metastructure was proposed to reduce the parasitic capacitance and resistance of the metasurfaces [80], as shown in figure 3*b*. This metasurface does not have well-defined meta-atoms, and the meta-atom network connection forms one unit. Therefore, when the gap is connected by high-concentration 2DEG, the entire metasurface resonates as a collective state, while the resonance frequency of this collective state tends to be extremely low. When the 2DEG is depleted, the meta-atom is interrupted by the gap, forming a meta-atom boundary, and an individual state can be induced whose resonance frequency is related to the resonance of a single meta-atom. The collective-individual state transition can be achieved by controlling the voltage, thereby shifting the resonance frequency and increasing the modulation depth to 93%. In addition, employing a non-traditional arrangement of meta-atoms can reduce the parasitic modes and increase the modulation speed to 3 GHz while the −3 dB bandwidth can reach up to 1 GHz. The metasurface can also be coded to control the modulation of specific discrete frequencies, and this technique can be applied in wireless communication and imaging. Both of these works control the on and off state of the gap of the resonant structure by changing the concentration of 2DEG, but the combination of 2DEG and the metasurface is not the only way. In addition, another 2DEG metasurface, whose focus is not on the control of the distribution of the 2DEG

but on integrating the metal–semiconductor–metal (MSM) 2DEG varactors with the metasurfaces to achieve a dynamic modulation of THz waves, was proposed by Nouman *et al*. in 2016 [79] (figure 3*c*). When the applied bias is low, the depletion region cannot pinch off the 2DEG. At this time, the 2DEG in the connected state is an equipotential surface, and the gate contact has a high capacitance. With the increase in the applied bias voltage, the 2DEG is pinched off by the Schottky depletion region, and the total capacitance of the device decreases. Therefore, the applied voltage increases, which reduces the total capacitance of the device and shifts the LC resonance frequency point, thereby achieving a modulation depth of 45% and insertion loss of 4.3 dB at 0.58 THz. The cavity structure can be used to increase the modulation depth. To clarify this mechanism, the team proposed a reflective active metasurface combining a Fabry–Perot cavity with a metasurface [91]. The associated transmission line model shows that the metal short-circuit surface on the back renders the input conductance of the metasurface cavity structure to be lower than that of the metasurface without a back metal. A smaller conductance corresponds to a larger change in the reflectivity, which increases the modulation depth. In addition, the cavity structure exhibits multiple resonance frequencies. Changing the admittance of the metasurface by using the voltage can lead to a shift in each resonance frequency, thereby leading to modulations at multiple frequencies. When the thickness of the substrate is 400 µm, the metasurface cavity has a modulation depth of 45.2% at 0.45 THz, which is 22.6 times higher than that of the non-cavity metasurfaces. The THz amplitude modulator based on the 2DEG metasurface can achieve high-speed continuous and effective modulation, but its processing mechanism is based on resistance transformation. Capacitance transformation is expected to enhance the coupling between the metasurface and the THz wave to improve the modulation performance. Subsequently, Keller *et al*. achieved ultra-strong coupling by combining a 2DEG with a switchable THz superconducting metamaterial, in the case involving a significantly modified capacitor material. This approach of coupling a metasurface to a 2DEG exhibits the possibility of transforming the superconducting properties [92]. Later, the authors combined yttrium–barium–copper oxide (YBCO) films and 2DEG with complementary split-ring resonators to form a high-temperature superconducting metasurface that can generate high-quality factor (up to $Q = 31$) resonances, as shown in figure 3*d*. When the sample is heated above the critical temperature, the superconducting state transforms into the normal conductive state, and the resonance is continuous and stable under the action of the magnetic field [93]. To integrate the active metasurface with other components suitable for THz systems, Singh & Sonkusale proposed an on-chip active metasurface combining a slot waveguide with 2DEG [78], as shown in figure 3*e*. The THz wave transmitted in the slot waveguide interacts with the 2DEG located below the channel. With a certain concentration of 2DEG as the lossy medium, the THz waves in the channel attenuate exponentially along the channel. When the 2DEG is exhausted by the applied bias, the attenuation of the THz wave in the slot waveguide is reduced, and the THz wave can be transmitted. By changing the concentration of the 2DEG, the channel state in the slot waveguide can be transformed to achieve broadband modulation and a modulation speed of more than 14 GHz. Through the combination of metasurface and 2DEG, the THz wide range phase modulation of THz has been achieved, breaking through the current situation that the phase shift of single-layer transmissive THz phase modulators is less than 90°, but it has the same problem as THz amplitude modulator.

Furthermore, recent work has proved that such a 2DEG metasurface cannot only modulate the amplitude of THz waves but can also achieve effective phase modulation [94]. In 2017, Zhou *et al*. [76] proposed a THz active metasurface combining an HEMT with the quadruple-split-ring metasurface, as shown in figure 4*a*. The 2DEG concentration at the split gap is controlled by the voltage. When the 2DEG concentration is high, the gap is connected without inducing an LC resonance. When the 2DEG is depleted, the disconnected gap and the metasurface structure generate an LC resonance, and the equivalent dielectric constant of the metasurface changes compared with the state without the LC resonance. Therefore, by realizing the conversion between resonant and non-resonant states by controlling the voltage, the equivalent dielectric constant of the metasurface can be changed, thereby changing the phase of the THz wave. The

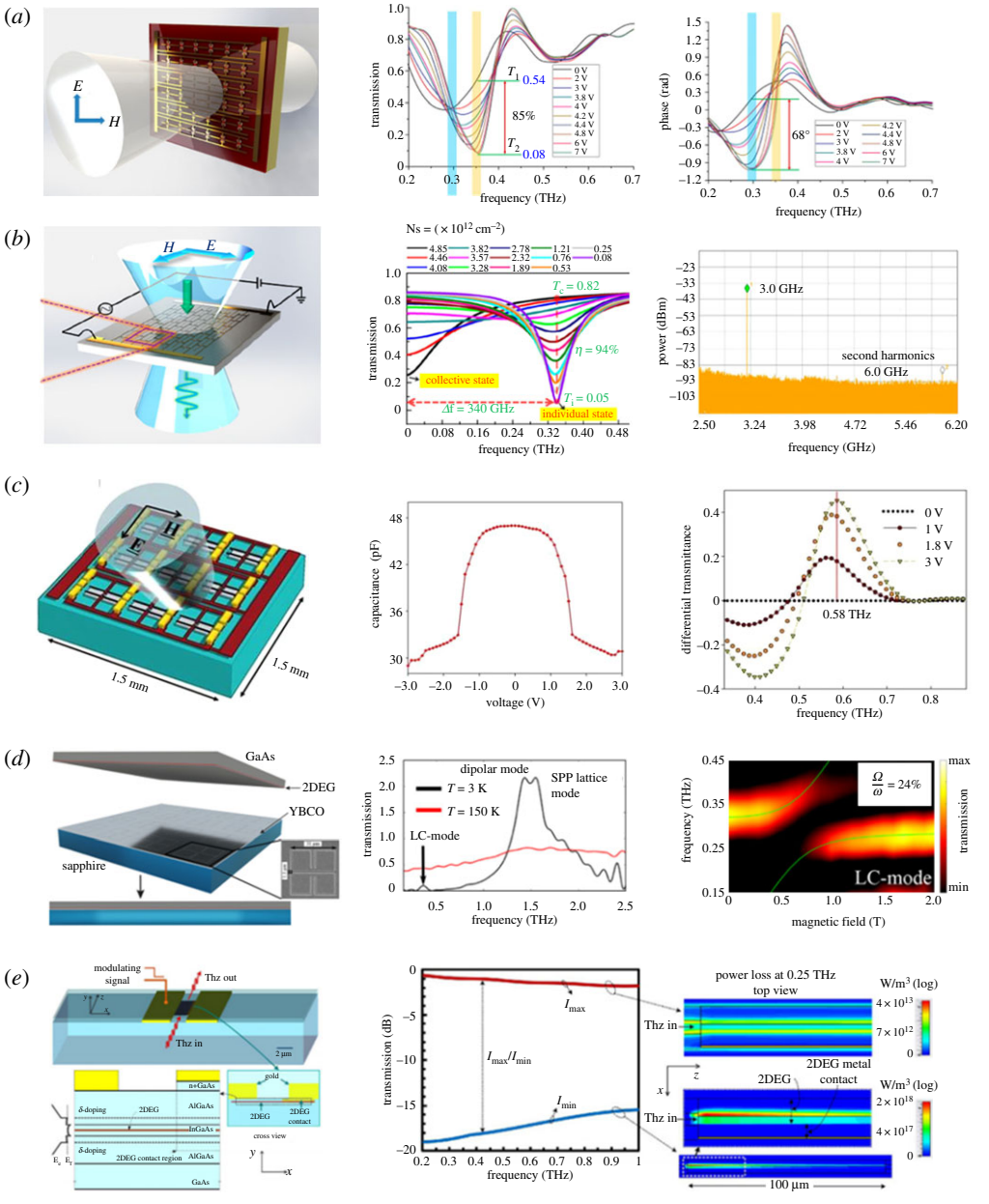

Figure 3. (*a*) Metasurface based on double-channel heterostructure, and its amplitude and phase modulation performance in experiments [69]. (*b*) Schematic of staggered netlike metasurface, and the transmission curve in simulation and dynamic test results [80]. (*c*) Structural diagram of the metasurface with 2DEG varactors, and its capacitance and transmission characteristics [79]. (*d*) Quadruple-split-ring metasurface and the experimental results [76]. (*e*) Schematic based on the enhanced resonant metasurface, and its transmission and phase characteristics in experiments [77]. (Online version in colour.)

active metasurface achieves a phase shift of 0.67 rad at 0.77 THz and a modulation speed of more than 2.7 MHz. Although the structure has a certain ability to modulate the phase of the THz wave, its phase modulation range needs to be further improved. In 2018, Zhang *et al*. [77] combined the enhanced resonant metallic structures and HEMT to achieve a large phase modulation, as shown in figure 4*b*. According to the Kramers–Kroenig (K–K) relationship, the amplitude and phase of a THz wave transmitted through a metasurface are not independent. By comparing the resonant

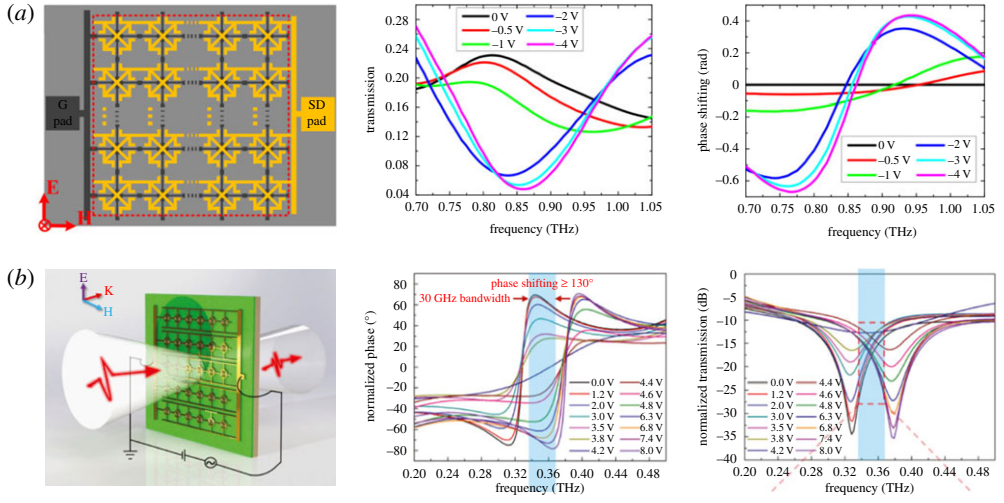

Figure 4. (*a*) Quadruple-split-ring metasurface and the experimental results [76]. (*b*) Schematic based on the enhanced resonant metasurface and its transmission and phase characteristics in experiments [77]. (Online version in colour.)

intensity and phase variation of multiple resonances, it is found that a larger phase jump exists near the resonant frequency of the stronger resonances. By applying an external voltage for the resonant mode conversion, this large phase active metasurface can achieve a phase shift of 137° at 0.352 THz. The 2DEG metasurface cannot only realize wavefront modulation, but can also be used as enhanced coupling.

Overall, the 2DEG metasurface has gradually become a promising means to realize high-performance smart and controllable devices owing to the convenient grid-control, 2DEG characteristics and various resonances of the metasurface. We believe that in the future, digital control circuits can be implemented to create increasingly smart devices by applying the 2DEG metasurface.

(c) Two-dimensional material and phase transition material film metasurface

Since 2D materials were first reported in 2004, they have provided a broad material platform for the development of reconfigurable smart metadevices [95–99]. The extraordinary properties of 2D materials, including the two-dimensional nature and ease of integration, enable them to be used in next-generation high-performance devices, which can enhance the performance of existing THz active metasurfaces [100]. As a typical 2D material, graphene is composed of carbon atoms arranged in a hexagonal lattice with a gapless, linear dispersion. Since the thickness of graphene (0.34 nm) is considerably smaller than the effective wavelength, the electromagnetic response of graphene mainly comes from charge carriers. Large mobility and amount of charge carriers in graphene have been reported, with value of up to 10^6 cm^2 (Vs)$^{-1}$ [101] and 10^{14} cm^2 [102], respectively. The light–matter interaction over a broad spectrum, from visible light to microwave, can be controlled by modulating the density of the free carriers [103,104]. Moreover, compared with the surface plasmons in metal, the plasmons in graphene have a longer excitation lifetime and can be effectively tuned, which make this configuration suitable for application in the THz field [105–107]. It has been theoretically and experimentally proved that graphene can be used for THz devices in different domains, such as by using active metasurfaces [108,109], and newer, better devices can be developed [110–118]. However, it is necessary to improve the relevant mechanism and manufacturing technique to obtain advanced industrially applicable devices.

Researchers have demonstrated the promising application of graphene-based metasurfaces. de Sterke *et al.* [119] reported on a polarization-independent ultrabroad bandwidth absorber based

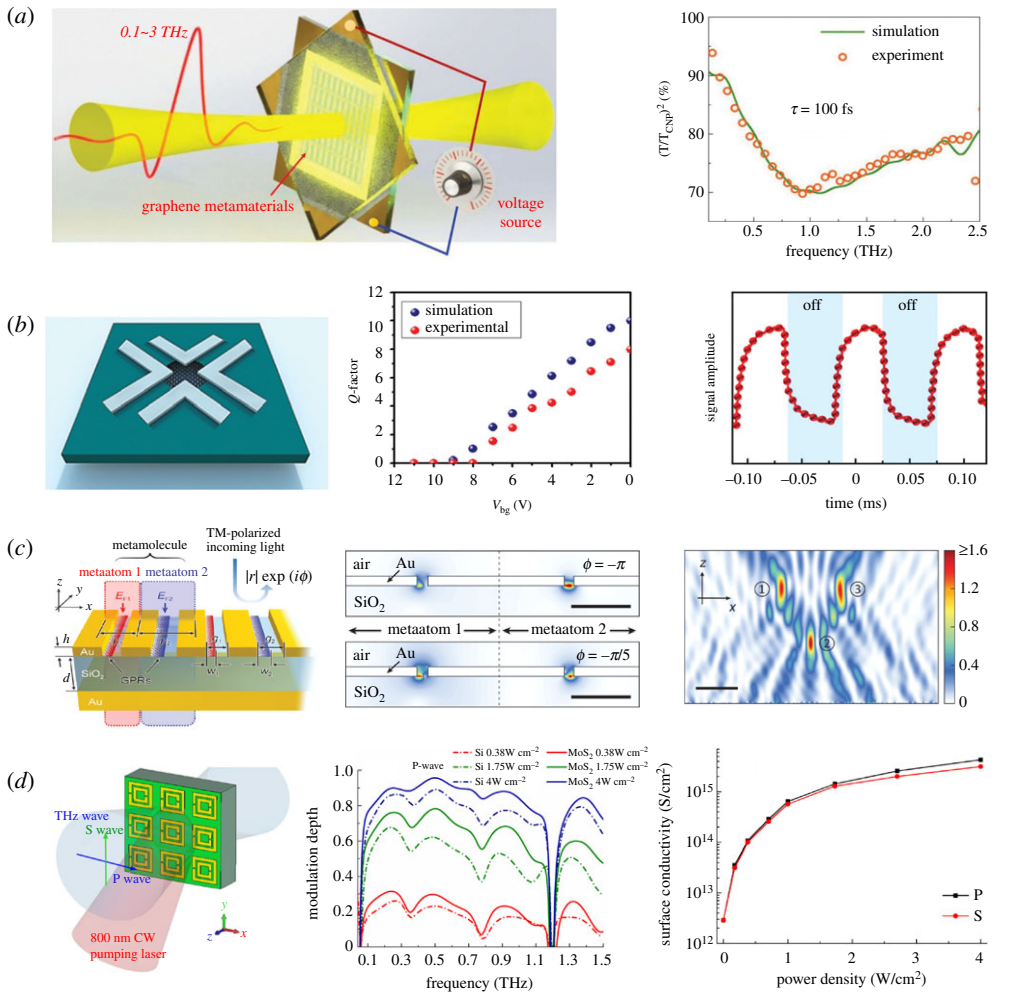

Figure 5. (*a*) Schematic of the device, and set-up of the experimental measurement; SEM image of the SRR structure; experimental and fitted transmission spectra with a relaxation time of 100 fs [81]. (*b*) Schematic of graphene island-mediated cluster structure; *Q* value and response optical signal in the experiment [82]. (*c*) Schematic of the proposed graphene plasmonic metamolecule; electric field distribution around the structure with a fixed amplitude; magnetic distribution with the beam spot triple focused to the specified location [120]. (*d*) Schematic of the MoS_2 metasurface; modulation depth in the metasurface and photoconductivity measured in the experiment [121]. (Online version in colour.)

on a multilayer graphene metamaterial consisting of alternating graphene and dielectric layers. This graphene metamaterial is patterned as a grating on a flexible substrate to ensure that the light can be coupled into the waveguide modes to retain a significant fraction of the energy in the metamaterial. The absorber achieves an absorptivity of 85% for the unpolarized light for incident angles of up to 60°, demonstrating a novel application of photonic devices based on multilayer graphene. Although it currently seems that multilayer graphene can achieve better modulation performance, due to the limitation of the fabrication, monolayer graphene is still the main research direction. In 2019, Yin *et al*. [81] experimentally demonstrated a graphene-based metamaterial whose modulation depth exceeds 35% by employing additional electrodes. In particular, the authors adopted a unique sandwich structure (figure 5*a*), which consisted of two patterned graphene metamaterial stacked face to face, with a spacer and a layer of ionic

liquid injected between them. The experimental results demonstrated a lifetime of show 100–200 fs and a low loss, thereby promoting the further development of graphene plasmon devices. In the same year, another team realized a higher performance with a modulation depth of 72% [82]. The authors proposed a graphene island-mediated THz plasmonic cluster to support plasmon resonance based on tunable charge transfer, as shown in figure 5*b*. The change in the conductivity of the graphene islands between the metal clusters enables positive control over the charge transitions of the entire component, making it possible to facilitate a high modulation depth THz active metasurface. In a recent study, Kim *et al.* [120] presented the 'metamolecule' concept, which couples THz waves to periodically arranged graphene plasmonic nanoresonators by using two independent meta-antennas. The Fermi level control of the graphene metamolecule ensures the complete tuning of the phase and amplitude of light, enabling a complete 2π phase shift and large amplitude modulation, as shown in figure 5*c*. Molybdenum disulfide (MoS_2), which is a typical transition metal dichalcogenide (TMD), has been studied extensively and noted to have properties and functions complementary to that of graphene in THz applications [122,123]. MoS_2 exhibits a direct bandgap semiconductor property in the monolayer form and can convert electrons into photons, making this material attractive for photoluminescence applications [124]. Compared with graphene, monolayer MoS_2 also has the characteristics of a monolayer atomic structure, high mobility and surface conductivity; however, the difference is that this material exhibits a direct band gap of 1.86 eV [124–127]. Cao *et al*. [128] reported a THz active metasurface based on multilayer MoS_2 and silicon with a modulation depth of 96% under a pump power of 4.56 W. Subsequently, Chang *et al.* [121] combined an MoS_2–Si heterostructure with a metallic metasurface, possessing a modulation depth of 90%, as shown in figure 5*d*. The authors reported that the modulation efficiency of a metasurface with MoS_2 is notably higher than that of a metasurface without MoS_2, and the maximum modulation efficiency can be achieved under a certain pumping power.

Compared with 2D materials, the ease of fabrication of phase transition materials make them another promising candidate to develop reconfigurable devices in the THz range [129–134]. VO_2 is a potential phase transition material, exhibiting an insulator-to-metal transition under certain conditions [135,136]. Accompanying the phase transition, the conductivity, magnetic susceptibility and light absorption of the material change abruptly, and the phase transition process is reversible. Due to the dramatic changes in its electrical and optical property [137], subpicosecond response time [138] and phase transition temperature being close to the room temperature [139], VO_2 has been considered for application in THz devices.

Combining reconfigurable metasurfaces with VO_2 is a widely used approach for THz active metasurfaces, which usually trigger the insulator-to-metal phase transition mechanisms by thermal heating [84,140], optical excitation [138,141,142] and electrical field application [83,143]. Zhang *et al*. [84] experimentally demonstrated that a meta-holography approach using a VO_2-integrated metasurface can be used to dynamically tune the overall holographic image. The metahologram is schematically illustrated in figure 6*a*, consisting of a passive set of metal SRR structures and an active set of SRRs integrated with VO_2. Both sets of structures generate special images with a pre-designed amplitude and phase distribution. When VO_2 changes from the dielectric phase to the metallic phase due to external heating, an image of the letter 'H' (at 25°C) can become that of 'G' (at 100°C), as shown in figure 6*b*. Compared with heating using an external heating element, switching induced by electrical current facilitates the easier integration of the devices. The SRRs can be combined with a metallic grid based on VO_2 to achieve the transmission modulation of a specific spectral band [83]. The grid plays the role of a microheater without affecting the resonance of the SRRs, enabling VO_2 to switch electrically (in figure 6*c*). With only a few volts of DC bias, the narrow-band switching behaviour is notable in each resonant mode. Optical excitation is another mechanism to control the insulator-to-metal phase transition of VO_2. By analysing the coupling resonance modes of various artificial microstructures, Zhang *et al*. designed a ring-dumbbell hybrid metasurface integrated with VO_2 to realize an average phase shift of 130° over 55 GHz, which has not been previously reported [70]. The resonant mode of the metasurface can be controlled by the phase transition of VO_2

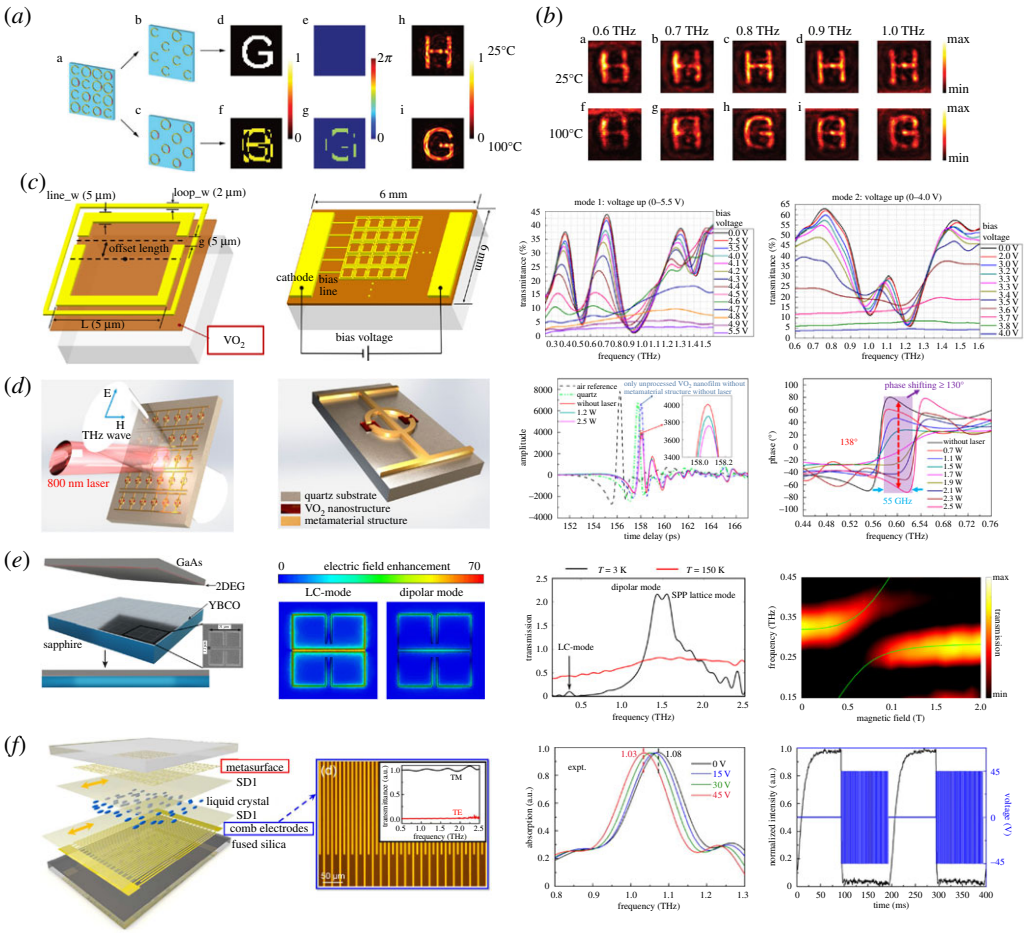

Figure 6. (*a*,*b*) The design mechanism and measured holographic images of the dynamic metasurface, respectively [84]. (*c*) Schematic of the VO_2 metasurface; transmittance of the VO_2 metasurface operated in modes 1 and 2 at various voltages [83]. (*d*) Three-dimensional schematic of the experiment and experimental time-domain data and phase spectra [70]. (*e*) Sketch of the YBCO metasurface; electric distribution of the LC and dipolar modes; electric field distribution under the LC and dipolar modes; relationship between the transmission spectra and magnetic field of the LC mode [93]. (*f*) Decomposition diagram of the metadevice; measured absorption spectra and the electro-optical response of the device [144]. (Online version in colour.)

with different laser powers, causing a significant phase shift of up to 138° at 0.6 THz, as shown in figure 6*d*. Subsequently, certain similar works were reported; however, the problem of high loss remains a key drawback for transmittance modulators [145]. In recent years, in addition to VO_2, other phase transition materials, such as superconductors, ferroelectrics and liquid crystals, have been integrated with metasurfaces to develop tunable THz devices. The high performance of superconductors originates from their low ohmic loss, high figure of merit and high sensitivity to external excitation [134,146–149]. In 2018, a high-temperature superconducting metasurface was proposed to yield a high Q resonance based on YBCO, as shown in figure 6*e* [93]. A stable resonance can be observed under an external magnetic field below the critical temperature of 9 T, owing to which, the ultra-strong coupling can be realized using a superconducting metasurface with Landau level transitions. Liquid crystal materials have a unique fluidity and a molecular order that is not found in other phase transition materials, and the dielectric anisotropy ranges from the ultraviolet to microwave domain [150–152]. For example, a liquid-crystal-integrated metadevice with versatile manipulations of THz waves has been developed [144]. The device

consists of a liquid crystal layer sandwiching a gold comb electrode and an array of SRR, as shown in figure 6*f*. For the reflection mode, this device can be applied as a perfect absorber, while for the transmission mode, the device behaves as an electromagnetically induced transparency analogue. The THz active metasurfaces of different active components show extraordinary modulation performance for THz wave amplitude and phase. We believe that with the development of THz technology, THz intelligent metasurfaces based on these active components will be designed to plump THz metasurfaces in the near future.

3. Applications for terahertz active metasurfaces

With the ongoing advancement in the THz active metasurface technology, the potential of such devices is being gradually highlighted. This section is structured in four subsections attending to the main application and prospects of THz active metasurface: high-speed wireless communication, non-destructive testing (NDT) and high-resolution imaging, biological detection and sensing, and prospects for future applications of THz active metasurfaces.

(a) Application of high-speed wireless communication

Due to their flexibility and multi-functional aspects, active metasurfaces can act as switches, modulators, beam-scanning devices and antennas in wireless communication application systems. Recently, a novel direct digital modulation wireless communication architecture based on an active metasurface was proposed [153]. Since the active metasurface can be controlled with an external voltage signal, each element can be coded as '0' and '1' digital meta-atoms to ensure that the digital information can be loaded on the metasurface to modulate the transmitted or reflected electromagnetic waves with the corresponding input signal (figure 7*a*). More importantly, the active metasurfaces can replace the digital–analogue convertor, antenna and series of active/passive devices, thereby simplifying the traditional communication system. Based on this novel concept, this active metasurface communication system is expanded to multichannel direct transmissions [154]. By coding and configuring the active metasurface, the digital information can be loaded on each element of the metasurfaces to construct a data transmission multichannel. In such a system, the active metasurface can act as an energy radiator, information modulator and information channel divider. More importantly, the active metasurface can be used for both spatial and temporal modulations, to realize the data transmission and multichannel division simultaneously, as shown in figure 7*b*. The FPGA can provide the coding schemes to the active metasurface. Consequently, the spatial modulation of the active metasurface can help construct the transmission channels, and the amplitude modulation on each channel can be applied to transmit the on–off key (OOK) digital information. This new communication architecture exhibits application potential in high-capacity communication with a low system complexity. Considering the internal connection of the metasurfaces, the use of artificial intelligence in combination with an active metasurface has been proposed to realize individual control of every single element and intercommunication with each other [156]. This aspect reflects the possibility of realization of an intelligent metasurface and intercell communication. Tasolamprou *et al*. studied the communication channels within an active metasurface and analysed various kinds of channels including layer communication, communication inside the metasurface and a dedicated parallel-plate waveguide. Although the path loss is relatively high, this work illustrated a vision for the intercommunication demand of smart active metasurfaces. The digital-coding and programming techniques can be combined to realize new functionalities of active metasurfaces and enable the development of intelligent metasurfaces. In 2019, Cui *et al.* [155] proposed a time-domain digital-coding mechanism applied to an active metasurface for application to a novel wireless communication system, which demonstrates the prospective application of the active metasurfaces to wireless communication. In contrast with the amplitude and phase modulation, by using time-domain coding, efficient manipulation of the spectral harmonic distribution can be achieved, which can further integrate

the concepts of space, frequency and time domains by using active metasurfaces. The basic principle pertains to the Fourier transform relation between time and frequency, which can be used to effectively modulate the signal. The QPSK real-time communication system has been realized based on the active metasurface, as shown in figure 7*c*. By programming the active metasurface, the reflection coefficient can be encoded; thus, the reflection coefficient can be coded in a definite sequence to load the baseband signal on the carrier wave. Furthermore, based on the active metasurface with time-domain digital-coding, another communication architecture has been proposed, in which multiple receiving antennas are applied to decode the received reflected radiation pattern. In this quasi-single input multiple output system, the transmitter consists of only the RF source and active metasurface, which is an extremely simple system. The FPGA is used to encode the active metasurface, while the reflected radiation can contain the entire digital information that can be recovered by realizing one-to-one mapping between the received radiation pattern and hardware code [153]. Overall, smart active metasurfaces can be applied to develop wireless communication techniques with considerably simpler and higher performance systems. Until now, these new communication systems have been realized in the microwave region; however, with the development of the THz active metasurface, these systems can be expanded to the THz region. In recent years, some results have been presented to develop active metasurface-based THz wireless communication systems [80]. The 2DEG active metasurfaces have been used to directly modulate the transmission rate of the incident free-space propagating THz wave to realize an OOK communication system. Similar to the systems working in the microwave frequency band, as mentioned previously, this system is also remarkably simple. Figure 7*d* shows the schematic of a THz wireless transmission system. The transmitter contains only the THz source based on the multi-chain, FPGA baseband and active metasurface. The analogue signal is converted into a baseband digital signal and loaded onto the active metasurface via a modulator drive module. The receiver is simply an envelope detector. This system operates at 0.34 THz, and the modulation rate is up to 3 GHz. Due to the limitation of the modulation speed of the modulator, at this stage, the transmission speed of this system cannot reach 10 Gbps. However, we believe that in the future, with the advancement of the active metasurface technology, metasurface communication systems can be developed to have higher speeds, lower system complexity and intelligence in the THz band.

(b) Application of non-destructive testing and high-resolution imaging

Terahertz NDT technology can be used to detect the hidden defects of most non-conductive materials. This technology is a powerful tool for biomedical imaging and has great significance for future intelligent medical treatment and industrial detection. Terahertz pulse imaging (TPI) can determine the properties of materials in the range of millimetre and submillimetre spectrum [157]. TPI system has a six-axis robot system, as shown in figure 8*a*, which can flexibly adjust the three-dimensional position of THz focus to carry out 3D non-destructive inspection of materials [158]. By employing a TPI system, non-destructive detection of different materials has been reported. In 2016, Ryu *et al*. [159] used THz spectroscopy to non-destructively evaluate the hidden multilayer structure of glass fibre-reinforced plastic composites. The imaging results show that, as shown in figure 8*b*, THz imaging clearly detects the layered interface (up), while the ultrasonic layered information detected by the ultrasonic imaging is blurred (down). In 2018, Zhong *et al.* [160] proposed a TPI imaging method to extract structural features of marine protective coatings. The results show that even in the presence of background noise, the micro defects hidden under the coating can be detected effectively. This method is beneficial to the detection of coating quality, the effective maintenance of coating and the avoidance of coating failure (figure 8*c*). THz NDT attracts significant attention, and many researchers are working to promote THz NDT technology. However, the relatively high cost of the TPI system limits its large-scale application. In addition, for THz high penetration NDT, a higher signal-to-noise ratio THz emission source is required. With progress in the THz imaging technology, several imaging techniques based on metasurfaces have been presented, such as phase-shift interferometry [164], compressed sensing [165] and

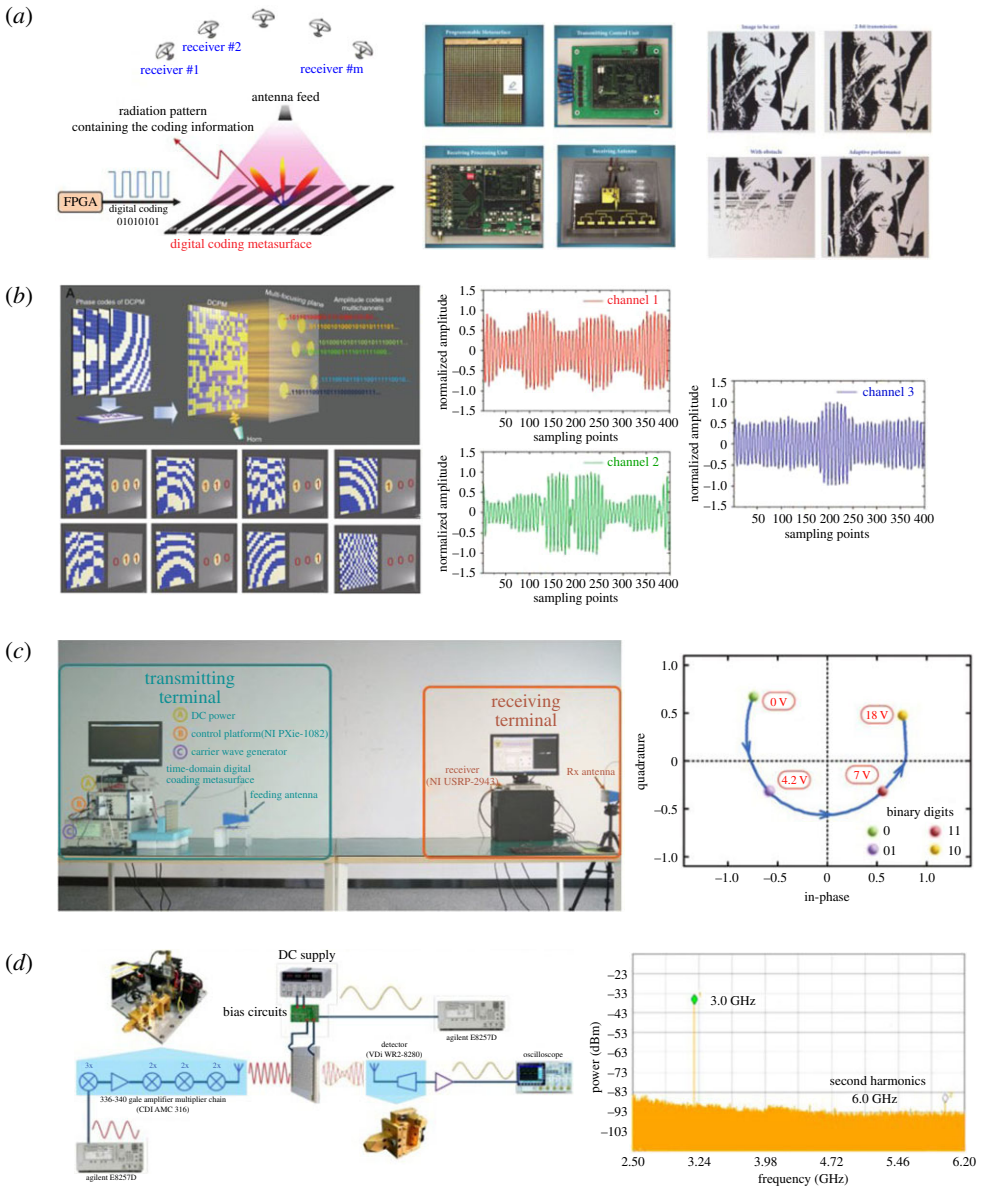

Figure 7. (*a*) Direct digital modulation wireless communication architecture [153]. (*b*) Multichannel near-field information direct transmission system, and the measured waveforms in the three channels [154]. (*c*) Wireless communication system based on time-domain digital metasurface [155]. (*d*) THz wireless transmission system, and the corresponding test results [80]. (Online version in colour.)

computational imaging [166]. Consequently, the active metasurface, which exhibits enormous potential in THz imaging, has become increasingly important in biological detection, medical diagnosis, security checks and radar systems. Thus, numerous kinds of imaging metasurfaces such as metalens, aperture metasurfaces and spatial light-active metasurface have been proposed to realize electromagnetic imaging with a high resolution, high tolerance and multicolour aspects.

A metalens consists of a particular static metasurface structure [167]. In principle, the metalens works similarly to an optical lens, except that they act on different frequencies of electromagnetic waves. Chen reported on an all-dielectric metalens set between the object and THz detector. This

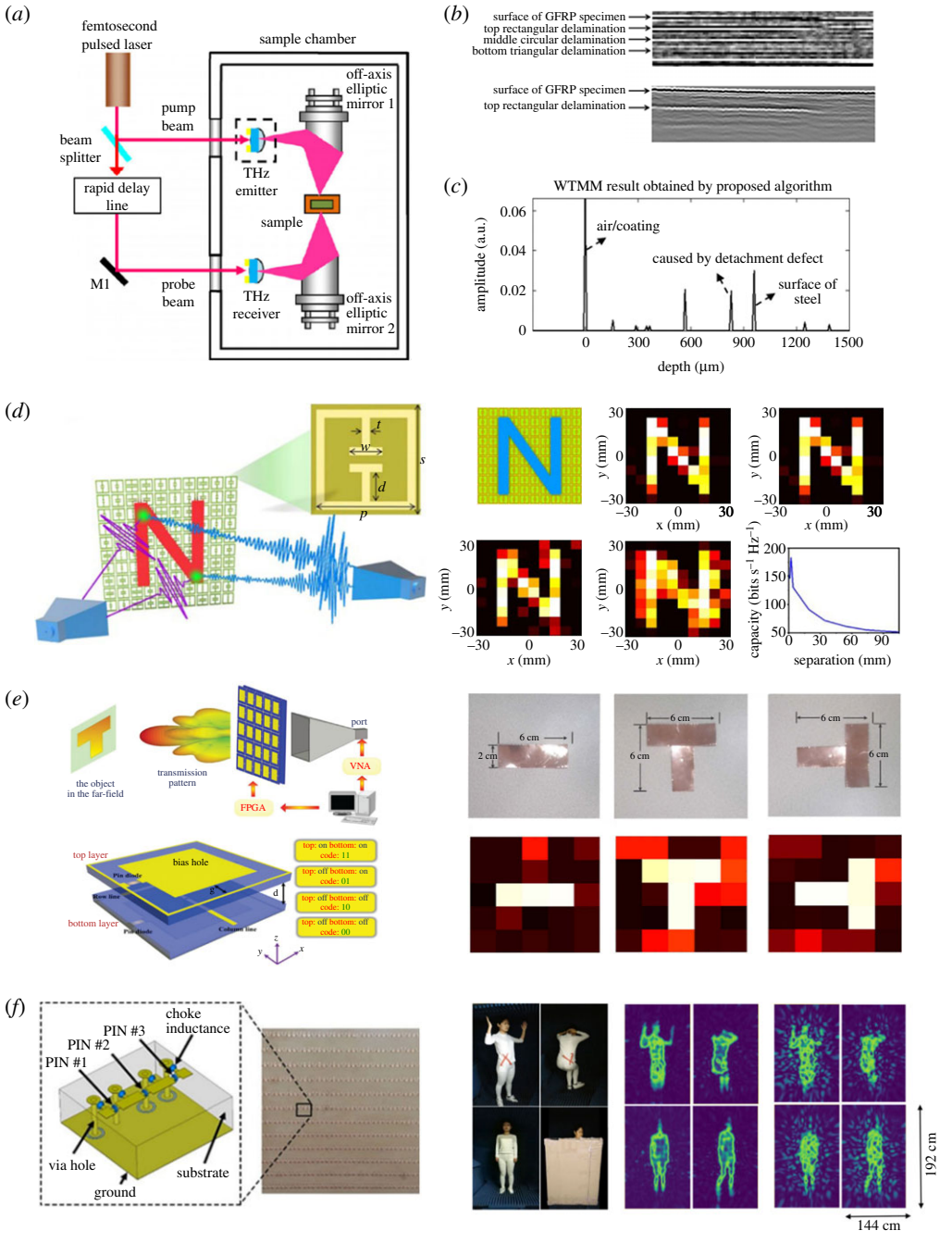

Figure 8. (*a*) Schematic of terahertz pulsed imaging (TPI) system [158]. (*b*) Multilayer composite imaged by THz and ultrasound [159]. (*c*) Marine protective coating test sample and TPI experimental results [160]. (*d*) Single-shot and single-sensor imaging system and subwavelength imaging in simulation [161]. (*e*) Transmission-type 2-bit active metasurface and imaging results [162]. (*f*) Active metasurface based on PIN diode and some images of different actions [163]. (Online version in colour.)

lens can transfer an image to the THz detector with a high optical efficiency [168]. By contrast, from the all-dielectric metalens, a metallic polarization-insensitive metalens can be set between the THz source and object. The metallic polarization-insensitive metalens performs as a booster

for the THz ray, enabling imaging with a longitudinal high tolerance owing to its extended focal depth [169]. However, lens imaging systems usually need to sample all pixels of the object, which perform low efficiency in measurement process. Therefore, a static metasurface aperture that allows for image compression with computational microwave imaging was proposed in 2013 [166]. This aperture metasurfaces uses the frequency diversity instead of the mechanical scanning to image. Its measurement just contains 101 values when the equivalent space-bandwidth product is 4475, representing a compression ratio of over 40 : 1. Subsequently, aperture active metasurfaces that do not require frequency diversity and need only an extremely narrow band of electromagnetic radiation were reported by Smith *et al.* [170]. The aperture active metasurfaces are made of a complementary electric LC resonator and diodes located at the gaps, thereby allowing the determination of dynamic microwave radiation patterns with different bias voltages. Consequently, imaging can be performed with a compression ratio of 10 : 1. Furthermore, the team of Smith improved the active metasurfaces working condition from a narrow-band to single-frequency domain [171]. By applying double 1D aperture active metasurfaces, 2D imaging with range and cross-range capacities can be realized. Recently, a single-shot and single-sensor imaging system with a spatial light-active metasurface was proposed, in which high-resolution imaging can be performed in the microwave band [161]. As shown in figure 8*d*, the imaging system includes two horn antennas as the single shot and single sensor, target object and spatio-temporal dispersive metasurface. The spatio-temporal dispersive metasurface, which consists of the FR4 substrate and electric LC resonator fabricated on both sides, allows the transfer of various wave components into the time domain efficiently. In the imaging process, a broadband electromagnetic wave is emitted from the single-shot antenna to the object, and the single sensor acquires the wave-data scattered from the object and reflected from the metasurface. After treating the acquired 1D temporal data by using a standard minimum least square reconstruction algorithm, some images of the objects, which can be clearly identified, are obtained. Subsequently, by taking advantage of the iteratively reweighting algorithm, some higher resolution images are achieved. Moreover, this system can be used for subwavelength imaging. Several images with different distances between the character 'N' and the metasurface are imaged in a simulation. The imaging quality gradually increases when the distance between the object and the metasurface reduces. This work demonstrates that the dispersive character of complex objects adversely influences the image quality. To address this issue, a transmission-type 2-bit active metasurface for microwave imaging was presented [162]. The transmission-type 2-bit active metasurface, as a two-layered structure, allows the control of the rows and columns in four states: '11', '01', '10' and '00', as shown in figure 8*e*. The '1' and '0' binary codes represent the 'on' and 'off' states of the diode fabricated on the two layers, respectively. The system can efficiently obtain the images of the target objects after calibrating the generalized system response matrix. In addition, this active metasurface can considerably reduce the cost and complexity of the imaging system because of the binary code control. Furthermore, the device works at a single frequency, which can eliminate the effect of object dispersion to improve the imaging quality. Presently, several novel techniques have been developed to realize high-accuracy imaging and real-time imaging by incorporating a programmable metasurface with machine learning [163] and neural networks [172]. Recently, Cui *et al.* [163] applied machine learning techniques to manipulate the radiation patterns by using a programmable metasurface. As shown in figure 8*f*, the phase and reflection amplitude of the programmable metasurface can be controlled using a PIN diode, which allows the generation of codes '00', '01', '10' and '11'. By employing a programmable metasurface with the principal component analysis and random projection machine learning training methods, real-time and high-quality images can be obtained in the case of 400 measurements with 8000 unknown pixels. Furthermore, when using the principal component analysis training theory, an acceptable image with a compression rate of 7.6% can be obtained with 60 measurements. Based on these outstanding achievements, the TPI system combined with the metasurface with a strong electromagnetic manipulation force is expected to reduce the cost of the NDT technology and improve the signal-to-noise ratio of the TPI.

(c) Application of biological detection and sensing

THz radiation has been proven to be a harmless detection technique for living organisms. THz detection has become a good choice for cancer and tumour treatment, because THz radiation is very sensitive to water and the water content of tumour cells is different from that of healthy cells. In addition, THz absorption is dominated by the unique intermolecular and weak interactions (such as van der Waals force) or intramolecular vibrations (such as hydrogen bonds), thus obtaining important information about the chemical composition of substances and biomolecules. Based on these characteristics, THz biological detection and sensing research has spread all over the world, covering protein concentration detection [173,174], DNA sequencing, detection of cancer cells and tumours [175–178], disease diagnosis [176] or detection of microorganisms [179,180], etc. However, it is still a challenge to obtain reliable sensing with a small amount sample [181]. In this case, it is difficult or impossible to detect applying traditional techniques, because the measured substance simply cannot interact sufficiently with the THz wave. As the most important index of THz biological detection and sensing, the sensitivity affects the accuracy and precision of biological information extraction. To overcome this issue, the THz biological detection and sensing technology based on metasurface provides an excellent solution. In addition to manipulating and modulating THz waves, metasurfaces also enhance or converge THz waves at specific locations, which ensures the interaction between THz waves and a small amount sample.

In 2004, using metasurface sensors for the first time in the infrared range, Brolo *et al*. [182] designed a nanopore array in gold film to monitor the binding of organic and biomolecules to metasurfaces. Generally, the interaction between a biological sample and a frequency-tunable plasmon is measured for medical examination, in which case different tissues may require different transmission spectra. In [183], Deng *et al*. proposed a spiral plasma structure consisting of a spiral bulls-eye antenna group and a subwavelength aperture surrounded by concentric grooves. Through this structure, it can be observed that the height of the transmission belt is adjustable, as shown in the illustration on the left panel of figure 9*a*. The main purpose of this work is to characterize different mouse tissues. To test the application of the device in biosensing, different mouse tissues (such as skin, heart, lung or brain samples) were cut into spirals. The transmission spectrum of the structure of the above sample is shown on the left side of figure 9*a*. As a result, the transmission peak of many samples can be observed in the frequency range of 1–1.3 THz. Park *et al*. [180] indicate that the transmission spectra of mouse bones and scalp are very different. Taking advantage of this, two cross-sections with a diameter of 2.5 mm were cut in the tail of the mouse for comparison (see the middle part of figure 9*a*). Then, a THz image is obtained by using a traditional mirror-based focus setting (upper right image of figure 9*a*) and a designed spiral bull's eye (lower right image of figure 9*a*). Due to the low resolution of traditional mirror-based focusing equipment, the measurement results show no difference between different tissues. However, when the sample is placed in a spiral structure, it can be clearly distinguished. Finally, a transmission image of the lungs of the rat was taken, and the biological 3D microstructure can be observed in the middle of the lung lobes. These experiments proved that the antenna has great value for medical examination through the spectrum, sensing and imaging in the THz range. The demand for tools to quickly and efficiently detect microorganisms such as fungi, bacteria or viruses is growing, because they are the cause of many human diseases. Some existing technologies are complex and difficult to apply to medical scenes. Metasurfaces have had a huge impact on them, so THz-based metasurfaces are a completely new choice. A metasurface-based sensor composed of a square ring metal array structure is introduced in [180]. In the left side of figure 9*b*, a gap is deposited in the centre of the metal ring above the Si substrate for ultrafast detection of live microorganisms. Due to the metasurfaces, the advantage of this type of structure over direct detection is that the size of the microorganism is very similar to the microgap of the resonator. Therefore, when the metasurfaces resonates, the microorganisms in the metal gap will have a high degree of interaction with the incident wave due to the high electric field strength present in this area, resulting in a significant change in frequency response. The advantage of sensing microorganisms

is that because the sensor surface can be cleaned, it can be re-used. When it is the same as the obtained spectrum measurement value, the structure is treated with a fungicide, and the obtained spectrum is returned to a position consistent with the original spectrum, as mentioned in [180]. To confirm that the technology can be extended to detect bacteria in the aquatic environment, the rear surface is functionalized by using receptors that detect certain bacteria. The following experiment was carried out to deposit *Escherichia coli* in a solution of 100 µg ml^{-1} on a design structure functionalized with *E. coli* antibodies. As shown in figure 9*b*, the structure is covered with a glass film while setting the thickness of the water layer to 55 µm by using an isolation layer. In 0.019 µm^{-2} *E. coli* solution, the THz transmission response shows a blue shift of 23 GHz. Because the dielectric constant of water (4.2) is higher than that of *E. coli* (1.6) in the THz range, it will move to a higher frequency. At the same time, the correct antibody should be used during the functionalization of the metasensor to create a structure that is sensitive to the desired microorganisms, because no changes are observed in the obtained spectrum without using *E. coli* antibodies when functionalizing the structure (see the right image of figure 9*b*). At the same time, under the same working dry environment, when the microbial count (N) of penicillin in the gap area changed from 0 to 5, multiple transmission spectra were obtained, and in all cases, a measurable frequency shift was obtained. It depends on the number of fungi and bacteria located in the metal hole area. In order to verify the obtained experimental results, different finite-difference time-domain simulations were carried out. The fungus was modelled as a sphere with a diameter of 2 µm and placed in the metal gap area of the structure. Consistent with the experimental results, an obvious frequency resonance red shift was observed (note that these results are not contradictory, because the dielectric constant of *E. coli* is lower than water and higher than air; therefore, in aqueous or dry environments, the blue shift or redshift). These results prove the effectiveness of the technology in biosensing applications. At the same time, the correct antibody should be used during the functionalization of the metasensor to create a structure that is sensitive to the desired microorganisms, because when functionalizing the structure, if no *E. coli* antibody is used, no changes are observed in the obtained spectrum. At the same time, in the study of the dry environment at work, the number of microorganisms (N) of penicillin in the gap area changed from 0 to 5, multiple transmission spectra were obtained, and a measurable frequency shift was obtained at all positions, due to the number of fungi and bacteria located in the metal hole area. The experimental results obtained in different time domains are verified by finite-difference simulation. Model the fungus as a sphere with a diameter of 2 µm and place it in the metal gap area of the structure. Obviously, a red shift of the resonance frequency can be observed (note that these results are not contradictory, because the dielectric constant of *E. coli* is lower than water and higher than air; therefore, in water or dry environments, the blue shift or red shift). It is consistent with the experimental results. These results prove the effectiveness of the technology in biosensing applications. In another study, the gap width of the structure was designed to vary between 0.2 and 3 µm. It can be found in the middle of figure 9*c* that the saturation of the response depends on the size of the gap. As the concentration increases, the dip angle will be red-shifted, and this rule applies to all situations. The results are clearly presented in the fourth and fifth columns of the right side of figure 9*c* and summarize the frequency shift of each gap width and surface density and the relationship between sensitivity and gap width. The frequency shift is reduced because it is placed in this area of viruses interaction, and the effect is relatively high. Therefore, it can be concluded that the sensitivity of the structure can be improved by optimizing the geometry of the metal pattern and the substrate. Good results have been obtained in [184], but because of the THz wave, the simulation is very expensive. Therefore, the topic of microbial sensing with metasurfaces is still a long-term research topic in the future.

(d) Prospects for future applications of terahertz active metasurfaces

Metasurfaces not only overcome the problems of high loss and difficult fabrication of bulk metamaterials but also realize powerful manipulation of EM waves and enhance the sensitivity of biological detection. Active metasurface combined with tunable components are expected to

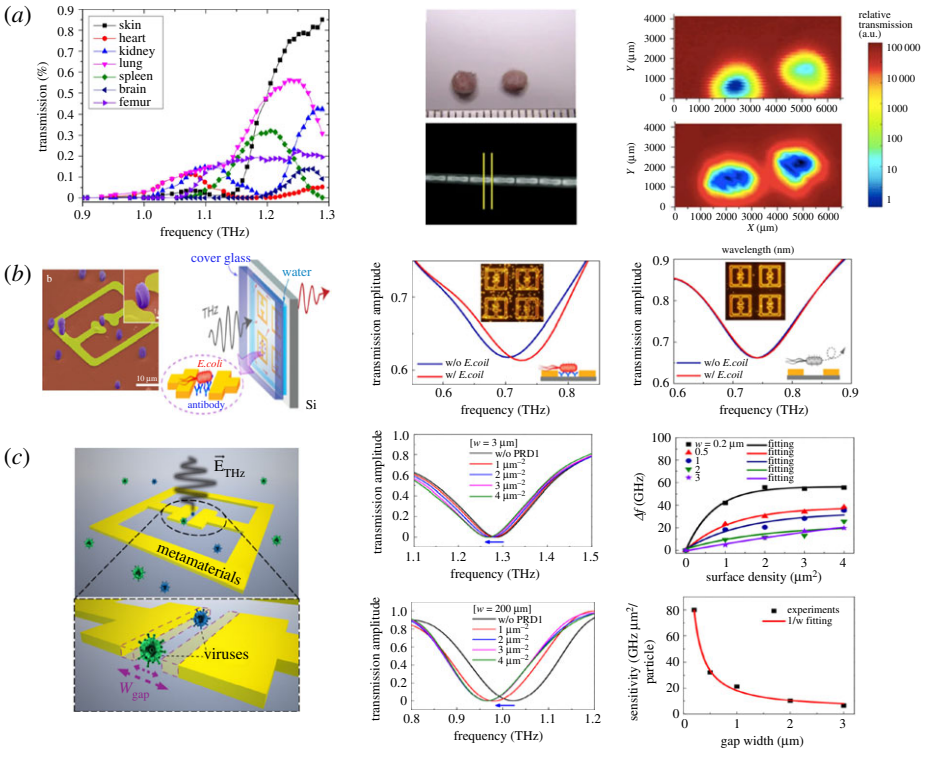

Figure 9. (*a*) The left side of the picture shows the THz transmission spectrum of different mouse tissues under the spiral structure. The mouse slice photo demonstrates the excised tail and slice position in the X-ray image (centre of figure). Using the traditional mirror-based focus setting (upper right of the picture) and the designed spiral bull's eye (lower right of the picture), the THz diagram of the mouse tail is shown [183]. (*b*) Microscope image of *E. coli* bacteria detector and metasurfaces (left side of the figure). On the functionalized structure (centre) and the unfunctionalized metasurfaces (right), the blue and red curves represent the THz transmission amplitude before and after *E. coli* deposition (right side of the figure) [180]. (*c*) The nano-gap metasurfaces and its metasurfaces enough to detect viruses (left side of the figure). Normalized transmission amplitude of the metasurfaces of PRD1 virus at different concentrations (in the middle of the figure). The frequency shift as a function of the gap size is different surface density (upper right of the figure). Sensitivity as a function of gap (bottom right of the figure) [184]. (Online version in colour.)

autonomously realize real-time beam scanning and tracking, fixed-point beam radiation, radar cross-section reduction and other functions. The future application of THz active metasurface is expected to be more abundant and practical (figure 10). Currently, cloud computing and terminal processing are effective processing methods for artificial intelligence. The terminal extracts a large amount of information and sends it to the artificial intelligence system in the cloud for unified processing. However, due to the limited network transmission capabilities, the current overall processing speed of artificial intelligence is low, resulting in a low degree of intelligence. Fifth-generation communication systems (5G), which apply microwave and millimetre waves as carriers, exhibit higher transmission speeds, lower communication delays, greater bandwidth and higher reliability. 5G technology is at the forefront of artificial intelligence, as it accelerates the algorithms and paves the way for the application of artificial intelligence. Smart metasurfaces manipulate microwave and millimetre waves intelligently, and this aspect is expected to connect 5G and artificial intelligence technologies. Such a framework provides a powerful information infrastructure for emerging industries such as 5G wireless systems, smart homes, intelligent monitoring, autonomous driving, Internet of things and smart industries. In the context of the future (6G) wireless communication technology, one possibility is to further improve the carrier

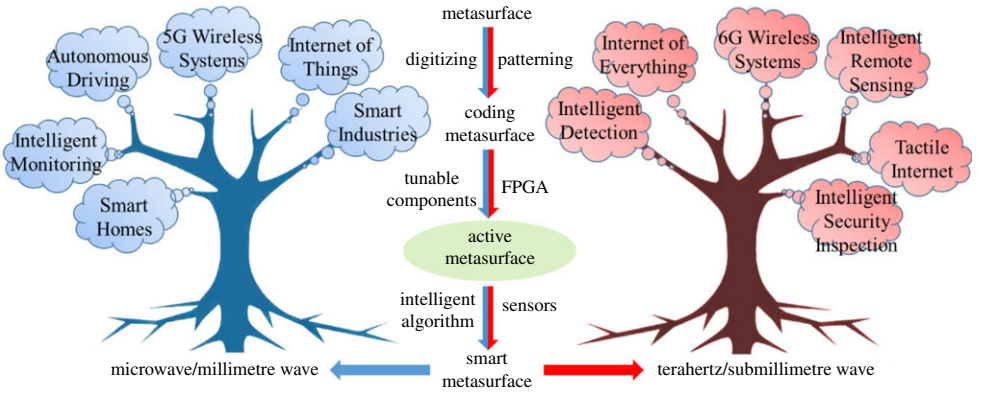

Figure 10. Prospective view of active and smart metasurfaces. (Online version in colour.)

frequency to meet the ever-expanding traffic demand of artificial intelligence. Adjacent to the millimetre-wave spectrum, the THz band exhibits considerable potential as a key requirement for the future 6G wireless intelligent systems [185]. The THz domain can provide bandwidth resources of tens to up to hundreds of GHz, which can support terabit-per-second data rates. The symbol duration is maintained at a picosecond level, thereby further reducing the network delay to the microsecond level. In addition, the THz band represents a transition from the macro-classical theory to micro-quantum theory, and it is also a transition from the electronics to photonics domain. This unique position pertains to a low photon energy, high transmission and unique absorption characteristics, which are not available in other frequency bands [186]. Therefore, THz active metasurfaces are expected to provide novel device support for 6G wireless systems, Internet of things and tactile Internet in the future, and they exhibit a unique significance for intelligent remote sensing, intelligent detection, intelligent security inspection and other such fields. Therefore, the realization of active metasurfaces is the most important step in the evolution of conventional metasurfaces to smart metasurfaces.

4. Conclusion

In this paper, the research progress of active metasurfaces with different tunable components and their applications in high-speed communication, NDT and biological are reviewed. The coding metamaterials exhibit a deeper internal relation between the phase distribution patterns and electromagnetic waves, which provides theoretical support for the digitization of artificial materials. Since the concept first emerged, certain unexpected gains have been made in the domains of beam steering, radar cross-section reduction, electromagnetic focusing, detection and other aspects. To satisfy the real-time application of metasurfaces in THz systems such as spectroscopy, imaging, beam scanning and high-speed communication, active metasurfaces with tunable components (diodes, two-dimensional electronic gases and other new materials) have been rapidly developed. Such metasurfaces play a key role in driving the development of THz high-speed communications and imaging technology, and many notable results have been achieved. More important, compared with the traditional non-destructive detection or biological detection, the THz detection-based metasurface has the powerful ability of energy manipulation, and it is easy to make matter interact with THz wave to enhance the precision detection. The high-speed dynamic controllable metasurfaces may replace the traditional mechanical chopper to realize high-speed lock-in amplification and 2D coding metasurface could bring extra matrix algorithm, which could improve the imaging resolution and the signal–noise ratio of the imaging system. Moreover, as mentioned in [187], the dynamic metasurface can provide more abundant dynamic modes, and can realize multiple modes of measurement or detection for the same

object, which is expected to further improve the detection or imaging accuracy and efficiency. Therefore, by applying the advantages of the coding metasurface, the traditional non-destructive detection or biological detection system could combine with sparse matrix technique, tunable focusing technique, beam-scanning technique and so on to realize higher performance. With the development of the relationship between the active metasurfaces and various signal processing operations, the active metasurface can be integrated with advanced artificial intelligence and deep learning algorithms to realize intelligent metasurfaces. Considering the current development trend of active metasurfaces, we expect that devices based on metasurfaces will play a key role in THz communication, NDT, imaging systems and biological detection, making THz systems adaptive and intelligent.

Data accessibility. This article has no additional data.

Authors' contributions. Z.Y. and Z.H. conceived the ideas in the paper. K.W. and W.L. assisted in writing the paper. Y.Z. and D.M.M. made key recommendations and amendments to the paper.

Competing interests. We declare we have no competing interests.

Funding. This work is supported by the The National Key Research and Development Program of China under contract no. 2018YFB1801503 and National Natural Science Foundation of China under contract nos. 61931006, 61741121 and 61771327.

References

1. Pendry JB, Holden AJ, Stewart WJ, Youngs I. 1996 Extremely low frequency plasmons in metallic mesostructures. *Phys. Rev. Lett.* **76**, 4773–4776. (doi:10.1103/PhysRevLett.76.4773)
2. Smith DR, Padilla WJ, Vier DC, Nemat-Nasser SC, Schultz S. 2000 Composite medium with simultaneously negative permeability and permittivity. *Phys. Rev. Lett.* **84**, 4184–4187. (doi:10.1103/PhysRevLett.84.4184)
3. Shelby RA, Smith DR, Schultz S. 2001 Experimental verification of a negative index of refraction. *Science* **292**, 77–79. (doi:10.1126/science.1058847)
4. Veselago VG, Narimanov EE. 2006 The left hand of brightness: past, present and future of negative index materials. *Nat. Mater.* **5**, 759–762. (doi:10.1038/nmat1746)
5. Smith DR, Pendry JB, Wiltshire MCK. 2004 Metamaterials and negative refractive index. *Science* **305**, 788–792. (doi:10.1126/science.1096796)
6. Liu R, Ji C, Mock JJJ, Chin JYY, Cui TJJ, Smith DRR. 2009 Broadband ground-plane cloak. *Science* **323**, 366–369. (doi:10.1126/science.1166949)
7. Freire MJ, Marqús R. 2005 Planar magnetoinductive lens for three-dimensional subwavelength imaging. *Appl. Phys. Lett.* **86**, 1–3. (doi:10.1063/1.1922074)
8. Landy NI, Sajuyigbe S, Mock JJ, Smith DR, Padilla WJ. 2008 Perfect metamaterial absorber. *Phys. Rev. Lett.* **100**, 207402. (doi:10.1103/PhysRevLett.100.207402)
9. Zhang S, Yin L, Fang N. 2009 Focusing ultrasound with an acoustic metamaterial network. *Phys. Rev. Lett.* **102**, 194301. (doi:10.1103/PhysRevLett.102.194301)
10. Liu S *et al.* 2016 Anisotropic coding metamaterials and their powerful manipulation of differently polarized terahertz waves. *Light Sci. Appl.* **5**, e16076. (doi:10.1038/lsa.2016.76)
11. Liu S, Chen H, Cui TJ. 2015 A broadband terahertz absorber using multi-layer stacked bars. *Appl. Phys. Lett.* **106**, 151601. (doi:10.1063/1.4918289)
12. Liu S *et al.* 2016 Frequency-dependent dual-functional coding metasurfaces at terahertz frequencies. *Adv. Opt. Mater.* **4**, 1965–1973. (doi:10.1002/adom.201600471)
13. Bai GD *et al.* 2018 Multitasking shared aperture enabled with multiband digital coding metasurface. *Adv. Opt. Mater.* **6**, 1800657. (doi:10.1002/adom.201800657)
14. Wu JW, Wu RY, Bo XC, Bao L, Fu XJ, Cui TJ. 2019 Synthesis algorithm for near-field power pattern control and its experimental verification via metasurfaces. *IEEE T. Antenn. Propag.* **67**, 1073–1083. (doi:10.1109/TAP.2018.2882645)
15. Yu N, Genevet P, Kats MA, Aieta F, Tetienne JPJ-P, Capasso F, Gaburro Z. 2011 Light propagation with phase discontinuities: generalized laws of reflection and refraction. *Science* **334**, 333–337. (doi:10.1126/science.1210713)

16. Cong X, Zhang L, Li J, Zhang M, Su H, Li IL, Ruan S, Liang H. 2019 Integration of ultrathin metasurfaces with a lens for efficient polarization division multiplexing. *Adv. Opt. Mater.* **7**, 1–7. (doi:10.1002/adom.201900116)
17. Zeng H *et al.* 2019 Terahertz dual-polarization beam splitter via an anisotropic matrix metasurface. *IEEE Trans. Terahertz Sci. Technol.* **9**, 491–497. (doi:10.1109/TTHZ.2019.2927890)
18. Liu K, Ge Y, Lin C. 2019 A compact wideband high-gain metasurface-lens-corrected conical horn antenna. *IEEE Antennas Wirel. Propag. Lett.* **18**, 457–461. (doi:10.1109/LAWP.2019.2894037)
19. Liang Y, Li B, Meng Z, Zhao L, Mao M, Liu H, Wei Z. 2020 Efficient point-by-point manipulated visible meta-vortex-lenses with arbitrary orbital angular momentum. *Nanotechnology* **31**, 035702. (doi:10.1088/1361-6528/ab4858)
20. Decker M, Chen WT, Nobis T, Zhu AY, Khorasaninejad M, Bharwani Z, Capasso F, Petschulat J. 2019 Imaging performance of polarization-insensitive metalenses. *ACS Photonics* **6**, 1493–1499. (doi:10.1021/acsphotonics.9b00221)
21. Yesilyurt O, Turhan-Sayan G. 2020 Metasurface lens for ultra-wideband planar antenna. *R. Soc. Open Sci.* **68**, 719–726. (doi:10.1109/TAP.2019.2940462)
22. Sung J, Lee GY, Lee B. 2019 Progresses in the practical metasurface for holography and lens. *Nanophotonics* **8**, 1701–1718. (doi:10.1515/nanoph-2019-0203)
23. Wang W, Zhao Z, Guo C, Guo K, Guo Z. 2019 Spin-selected dual-wavelength plasmonic metalenses. *Nanomaterials* **9**, 1–10. (doi:10.3390/nano9050761)
24. Legaria S, Pacheco-Peña V, Beruete M. 2018 Super-oscillatory metalens at terahertz for enhanced focusing with reduced side lobes. *Photonics* **5**, 10–16. (doi:10.3390/photonics5040056)
25. Wang H, Liu L, Lu X, Lü H, Han Y, Wang S, Teng S. 2018 Spatial multiplexing plasmonic metalenses based on nanometer cross holes. *New J. Phys.* **20**, 123009. (doi:10.1088/1367-2630/aaf4d6)
26. Abbaszadeh A, Ahmadi-Boroujeni M, Tehranian A. 2020 A compact polarization insensitive all-dielectric metasurface lens for Gaussian to tophat beam shaping in sub-terahertz regime. *Opt. Commun.* **462**, 125313. (doi:10.1016/j.optcom.2020.125313)
27. Zhang X, Kong D, Li S, Wang L. 2018 Generation of vortex beams with multi topological charges, high purity and operating on broadband using a simple silver metasurface. *Optik* **175**, 319–327. (doi:10.1016/j.ijleo.2018.09.003)
28. Tang S, Cai T, Wang GM, Liang JG, Li X, Yu J. 2018 High-efficiency dual-modes vortex beam generator with polarization-dependent transmission and reflection properties. *Sci. Rep.* **8**, 1–10. (doi:10.1038/s41598-018-24929-4)
29. Huang HF, Li SN. 2019 High-efficiency planar reflectarray with small-size for OAM generation at microwave range. *IEEE Antennas Wirel. Propag. Lett.* **18**, 432–436. (doi:10.1109/LAWP.2019.2893321)
30. Ran Y, Liang J, Cai T, Ji W, Wang G. 2018 High-performance broadband vortex beam generator based on double-layered reflective metasurface. *AIP Adv.* **8**, 095201. (doi:10.1063/1.5026888)
31. Ji C, Song J, Huang C, Wu X, Luo X. 2019 Dual-band vortex beam generation with different OAM modes using single-layer metasurface. *Opt. Express* **27**, 34. (doi:10.1364/oe.27.000034)
32. Heiden JT, Ding F, Linnet J, Yang Y, Beermann J, Bozhevolnyi SI. 2019 Gap-surface plasmon metasurfaces for broadband circular-to-linear polarization conversion and vector vortex beam generation. *Adv. Opt. Mater.* **7**, 1–9. (doi:10.1002/adom.201801414)
33. Akram MR, Mehmood MQ, Bai X, Jin R, Premaratne M, Zhu W. 2019 High efficiency ultrathin transmissive metasurfaces. *Adv. Opt. Mater.* **7**, 1–7. (doi:10.1002/adom.201801628)
34. Zang XF *et al.* 2019 Manipulating terahertz plasmonic vortex based on geometric and dynamic phase. *Adv. Opt. Mater.* **7**, 1–7. (doi:10.1002/adom.201801328)
35. Zhang C, Deng L, Zhu J, Hong W, Wang L, Yang W, Li S. 2018 Control of the spin angular momentum and orbital angular momentum of a reflected wave by multifunctional graphene metasurfaces. *Materials* **11**, 1054. (doi:10.3390/ma11071054)
36. Dharmavarapu R *et al.* 2019 Corrigendum: Dielectric cross-shaped-resonator-based metasurface for vortex beam generation at mid-IR and THz wavelengths (*Nanophotonics* (2019) 8:7 (1263–1270) doi:10.1515/nanoph-2019-0112). *Nanophotonics* **8**, 1263–1270. (doi:10.1515/nanoph-2019-0421)

37. Zhang B *et al.* 2019 Particle swarm optimized polarization beam splitter using metasurface-assisted silicon nitride Y-junction for mid-infrared wavelengths. *Opt. Commun.* **451**, 186–191. (doi:10.1016/j.optcom.2019.06.057)
38. Li J, Liu C, Wu T, Liu Y, Wang Y, Yu Z, Ye H, Yu L. 2019 Efficient polarization beam splitter based on all-dielectric metasurface in visible region. *Nanoscale Res. Lett.* **14**, 0–6. (doi:10.1186/s11671-019-2867-4)
39. Yang H, Ou K, Cao G, Shang X, Liu Y, Deng Y. 2019 Polarization beam splitter with disparate functionality in transmission and reflection modes. *Opt. Commun.* **443**, 104–109. (doi:10.1016/j.optcom.2019.03.022)
40. Tao C, Itoh T. 2019 Non-periodic metasurface beam splitter for dual polarizations. In 2019 49th European Microwave Conference, EuMC 2019, pp. 670–673. (doi:10.23919/EuMC.2019.8910674)
41. Zhang X, Davis JE, Güney DÖ. 2019 Ultra-thin metamaterial beam splitters. *Appl. Sci.* **10**, 53. (doi:10.3390/app10010053)
42. Lee WSL, Nirantar S, Headland D, Bhaskaran M, Sriram S, Fumeaux C, Withayachumnankul W. 2018 Broadband terahertz circular-polarization beam splitter. *Adv. Opt. Mater.* **6**, 1–7. (doi:10.1002/adom.201700852)
43. Chen M, Zhao D, Cai J, Wang C, Xiao X, Chang L. 2018 All-dielectric metasurfaces for circularly polarized beam-splitters with high conversion efficiency and broad bandwidth. *Optik* **165**, 41–49. (doi:10.1016/j.ijleo.2018.01.059)
44. Cui TJ, Qi MQ, Wan X, Zhao J, Cheng Q. 2014 Coding metamaterials, digital metamaterials and programmable metamaterials. *Light Sci. Appl.* **3**, e218. (doi:10.1038/lsa.2014.99)
45. Gao LH *et al.* 2015 Broadband diffusion of terahertz waves by multi-bit coding metasurfaces. *Light Sci. Appl.* **4**, e324. (doi:10.1038/lsa.2015.97)
46. Zhao J, Cheng Q, Wang TQ, Yuan W, Cui TJ. 2017 Fast design of broadband terahertz diffusion metasurfaces. *Opt. Express* **25**, 958–964. (doi:10.1364/OE.25.001050)
47. Zhang H, Lu Y, Su J, Li Z, Liu J, Yang Y. 2017 Coding diffusion metasurface for ultra-wideband RCS reduction. *Electron. Lett.* **53**, 187–189. (doi:10.1049/el.2016.3956)
48. Han J, Cao X, Gao J, Li S, Yang H, Zhang C, Li T. 2019 Broadband dual-circular polarized coding metasurfaces and their powerful manipulation of differently circular polarizations. *Opt. Express* **27**, 34141. (doi:10.1364/oe.27.034141)
49. Ali L, Li Q, Khan TA, Yi J, Chen X. 2019 Wideband RCS reduction using coding diffusion metasurface. *Materials* **12**, 1–11. (doi:10.3390/ma12172708)
50. Saifullah Y, Waqas AB, Yang G-M, Xu F. 2020 Multi-bit dielectric coding metasurface for EM wave manipulation and anomalous reflection. *Opt. Express* **28**, 1139. (doi:10.1364/oe.383214)
51. Guo W-L, Wang G-M, Hou H-S, Chen K, Feng Y. 2019 Multi-functional coding metasurface for dual-band independent electromagnetic wave control. *Opt. Express* **27**, 19196. (doi:10.1364/oe.27.019196)
52. Zhang L, Wu RY, Bai GD, Wu HT, Ma Q, Chen XQ, Cui TJ. 2018 Transmission-reflection-integrated multifunctional coding metasurface for full-space controls of electromagnetic waves. *Adv. Funct. Mater.* **28**, 1802205. (doi:10.1002/adfm.201802205)
53. Shao L, Premaratne M, Zhu W. 2019 Dual-functional coding metasurfaces made of anisotropic all-dielectric resonators. *IEEE Access* **7**, 45 716–45 722. (doi:10.1109/ACCESS.2019.2908830)
54. Liu S, Jun Cui T, Noor A, Tao Z, Chi Zhang H, Dong Bai G, Yang Y, Yang Zhou X. 2018 Negative reflection and negative surface wave conversion from obliquely incident electromagnetic waves. *Light Sci. Appl.* **7**, 18 008–18 011. (doi:10.1038/lsa.2018.8)
55. Deng ZL, Li G. 2017 Metasurface optical holography. *Mater. Today Phys.* **3**, 16–32. (doi:10.1016/j.mtphys.2017.11.001)
56. Zhang X, Pu M, Guo Y, Jin J, Li X, Ma X, Luo J, Wang C, Luo X. 2019 Colorful metahologram with independently controlled images in transmission and reflection spaces. *Adv. Funct. Mater.* **29**, 1–8. (doi:10.1002/adfm.201809145)
57. Yao M, Li JL. 2019 Beam reconfigurable holographic artificial impedance surface at terahertz band. *J. Phys. D: Appl. Phys.* **52**, 155001. (doi:10.1088/1361-6463/aafe5d)
58. Liu D, Wu J, Guo S. 2018 The generation of three-dimensional curved beams based on holographic metasurface. *Opt. Express* **26**, 22348. (doi:10.1364/oe.26.022348)
59. Zhang X *et al.* 2018 All-dielectric meta-holograms with holographic images transforming longitudinally. *ACS Photonics* **5**, 599–606. (doi:10.1021/acsphotonics.7b01173)

60. Burch J, Ma J, Hunter RI, Schulz SA, Robertson DA, Smith GM, Wang J, DI Falco A. 2019 Flexible patches for mm-wave holography. *Appl. Phys. Lett.* **115**, 021104. (doi:10.1063/1.5109627)
61. Deng J *et al.* 2019 Spatial frequency ultiplexed meta-holography and meta-nanoprinting. *ACS Nano* **13**, 9237–9246. (doi:10.1021/acsnano.9b03738)
62. Jiang Q, Jin G, Cao L. 2019 When metasurface meets hologram: principle and advances. *Adv. Opt. Photon.* **11**, 518. (doi:10.1364/aop.11.000518)
63. Wang Q, Plum E, Yang Q, Zhang X, Xu Q, Xu Y, Han J, Zhang W. 2018 Reflective chiral meta-holography: multiplexing holograms for circularly polarized waves. *Light: Sci. Appl.* **7**, 1–9. (doi:10.1038/s41377-018-0019-8)
64. Sengupta K, Nagatsuma T, Mittleman DM. 2018 Terahertz integrated electronic and hybrid electronic–photonic systems. *Nat. Electron.* **1**, 622. (doi:10.1038/s41928-018-0173-2)
65. Chen HT, Padilla WJ, Zide JMO, Gossard AC, Taylor AJ, Averitt RD. 2006 Active terahertz metamaterial devices. *Nature* **444**, 597–600. (doi:10.1038/nature05343)
66. Huang Y, Zhong S, Yao H, Cui D. 2017 Tunable terahertz plasmonic sensor based on graphene/insulator stacks. *IEEE Photonics J.* **9**, 1–10. (doi:10.1109/JPHOT.2017.2656242)
67. Zhang X, Xing Y, Zhang Q, Gu Y, Su Y, Ma C. 2018 High speed terahertz modulator based on the single channel AlGaN/GaN high electron mobility transistor. *Solid-State Electron.* **146**, 9–12. (doi:10.1016/j.sse.2018.04.011)
68. Huang Y, Zhong S, Shen Y, Yao L, Yu Y, Cui D. 2017 Graphene/insulator stack based ultrasensitive terahertz sensor with surface plasmon resonance. *IEEE Photonics J.* **9**, 1–11. (doi:10.1109/JPHOT.2017.2765182)
69. Zhang Y *et al.* 2015 Gbps terahertz external modulator based on a composite metamaterial with a double-channel heterostructure. *Nano Lett.* **15**, 3501–3506. (doi:10.1021/acs.nanolett.5b00869)
70. Zhao Y, Zhang Y, Shi Q, Liang S, Huang W, Kou W, Yang Z. 2018 Dynamic photoinduced controlling of the large phase shift of terahertz waves via vanadium dioxide coupling nanostructures. *ACS Photonics* **5**, 3040–3050. (doi:10.1021/acsphotonics.8b00276)
71. Huang Y, Zhong S, Shi T, Shen Y-C, Cui D. 2019 Trapping waves with tunable prism-coupling terahertz metasurfaces absorber. *Opt. Express* **27**, 25647. (doi:10.1364/oe.27.025647)
72. Huang Y, Zhong S, Shi T, Shen Y-C, Cui D. 2019 HR-Si prism coupled tightly confined spoof surface plasmon polaritons mode for terahertz sensing. *Opt. Express* **27**, 34067. (doi:10.1364/OE.27.034067)
73. Shrekenhamer D, Montoya J, Krishna S, Padilla WJ. 2013 Four-color metamaterial absorber THz spatial light modulator. *Adv. Opt. Mater.* **1**, 905–909. (doi:10.1002/adom.201300265)
74. Karl N, Reichel K, Chen H-T, Taylor AJ, Brener I, Benz A, Reno JL, Mendis R, Mittleman DM. 2014 An electrically driven terahertz metamaterial diffractive modulator with more than 20 dB of dynamic range. *Appl. Phys. Lett.* **104**, 091115. (doi:10.1063/1.4867276)
75. Su X *et al.* 2015 Active metasurface terahertz deflector with phase discontinuities. *Opt. Express* **23**, 27152. (doi:10.1364/oe.23.027152)
76. Zhou Z, Wang S, Yu Y, Chen Y, Feng L. 2017 High performance metamaterials-high electron mobility transistors integrated terahertz modulator. *Opt. Express* **25**, 17832. (doi:10.1364/oe.25.017832)
77. Zhang Y *et al.* 2018 Large phase modulation of THz wave via an enhanced resonant active HEMT metasurface. *Nanophotonics* **8**, 153–170. (doi:10.1515/nanoph-2018-0116)
78. Singh PK, Sonkusale S. 2017 High speed terahertz modulator on the chip based on tunable terahertz slot waveguide. *Sci. Rep.* **7**, 1–8. (doi:10.1038/srep40933)
79. Nouman MT, Kim HW, Woo JM, Hwang JH, Kim D, Jang JH. 2016 Terahertz modulator based on metamaterials integrated with metal-semiconductor-metal varactors. *Sci. Rep.* **6**, 1–7. (doi:10.1038/srep26452)
80. Zhao Y *et al.* 2019 High-speed efficient terahertz modulation based on tunable collective-individual state conversion within an active 3 nm two-dimensional electron gas metasurface. *Nano Lett.* **19**, 7588–7597. (doi:10.1021/acs.nanolett.9b01273)
81. Ye T, Wang B, Wang C, Li Z, Zhang Z, Jin K, Wang L, Yin Y. 2019 Approaching the intrinsic lifetime and modulating a graphene plasmonic resonance at a few hundred GHz. *Adv. Opt. Mater.* **7**, 1900315. (doi:10.1002/adom.201900315)

82. Ahmadivand A, Gerislioglu B, Ramezani Z. 2019 Gated graphene island-enabled tunable charge transfer plasmon terahertz metamodulator. *Nanoscale* **11**, 8091–8095. (doi:10.1039/c8nr10151e)
83. Park DJ, Shin JH, Park KH, Ryu HC. 2018 Electrically controllable THz asymmetric split-loop resonator with an outer square loop based on VO_2. *Opt. Express* **26**, 17397. (doi:10.1364/oe.26.017397)
84. Liu X *et al.* 2019 Thermally dependent dynamic meta-holography using a vanadium dioxide integrated metasurface. *Adv. Opt. Mater* **7**, 1900175. (doi:10.1002/adom.201900175)
85. Isić G, Vasić B, Zografopoulos DC, Beccherelli R, Gajić R. 2015 Electrically tunable critically coupled terahertz metamaterial absorber based on nematic liquid crystals. *Phys. Rev. Appl.* **3**, 064007. (doi:10.1103/PhysRevApplied.3.064007)
86. Watts CM, Shrekenhamer D, Montoya J, Lipworth G, Hunt J, Sleasman T, Krishna S, Smith DR, Padilla WJ. 2014 Terahertz compressive imaging with metamaterial spatial light modulators. *Nat. Photonics* **8**, 605–609. (doi:10.1038/nphoton.2014.139)
87. Chan WL, Charan K, Takhar D, Kelly KF, Baraniuk RG, Mittleman DM. 2008 A single-pixel terahertz imaging system based on compressed sensing. *Appl. Phys. Lett.* **93**, 121105. (doi:10.1063/1.2989126)
88. Karl N *et al.* 2017 Characterization of an active metasurface using terahertz ellipsometry. *Appl. Phys. Lett.* **111**, 191101. (doi:10.1063/1.5004194)
89. Shrekenhamer D, Rout S, Strikwerda AC, Bingham C, Averitt RD, Sonkusale S, Padilla WJ. 2011 High speed terahertz modulation from metamaterials with embedded high electron mobility transistors. *Opt. Express* **19**, 9968. (doi:10.1364/oe.19.009968)
90. Huang YD, Yu Y, Qin H, Sun JD, Zhang ZP, Li XX, Huang JJ, Cai Y. 2016 Plasmonic terahertz modulator based on a grating-coupled two-dimensional electron system. *Appl. Phys. Lett.* **109**, 201110. (doi:10.1063/1.4967998)
91. Lee G, Nouman MT, Hwang JH, Kim HW, Jang JH. 2018 Enhancing the modulation depth of a dynamic terahertz metasurface by integrating into an asymmetric Fabry-Pérot cavity. *AIP Adv.* **8**, 095310. (doi:10.1063/1.5034028)
92. Keller J, Maissen C, Scalari G, Beck M, Cibella S, Leoni R, Faist J. 2017 Combining a fully switchable THz superconducting metamaterial with a 2DEG for ultra-strong coupling. *Eur. Phys. J. Plus* **132**, 2015–2018. (doi:10.1140/epjp/i2017-11731-2)
93. Keller J, Scalari G, Appugliese F, Mavrona E, Rajabali S, Süess MJ, Beck M, Faist J. 2018 High Tc superconducting THz metamaterial for ultrastrong coupling in a magnetic field. *ACS Photonics* **5**, 3977–3983. (doi:10.1021/acsphotonics.8b01025)
94. Chen HT, Padilla WJ, Cich MJ, Azad AK, Averitt RD, Taylor AJ. 2009 A metamaterial solid-state terahertz phase modulator. *Nat. Photonics* **3**, 148–151. (doi:10.1038/nphoton.2009.3)
95. Sensale-Rodriguez B, Yan R, Kelly MM, Fang T, Tahy K, Hwang WS, Jena D, Liu L, Xing HG. 2012 Broadband graphene terahertz modulators enabled by intraband transitions. *Nat. Commun.* **3**, 780. (doi:10.1038/ncomms1787)
96. Sensale-Rodriguez B, Fang T, Yan R, Kelly MM, Jena D, Liu L, Xing H. 2011 Unique prospects for graphene-based terahertz modulators. *Appl. Phys. Lett.* **99**, 113104. (doi:10.1063/1.3636435)
97. Sensale-Rodriguez B, Yan R, Liu L, Jena D, Xing HG. 2013 Graphene for reconfigurable terahertz optoelectronics. *Proc. IEEE* **101**, 1705–1716. (doi:10.1109/JPROC.2013.2250471)
98. Ju L *et al.* 2011 Graphene plasmonics for tunable terahertz metamaterials. *Nat. Nanotechnol.* **6**, 630–634. (doi:10.1038/nnano.2011.146)
99. Tassin P, Koschny T, Soukoulis CM. 2013 Graphene for terahertz applications. *Science* **341**, 620–621. (doi:10.1126/science.1242253)
100. Lee SH *et al.* 2012 Switching terahertz waves with gate-controlled active graphene metamaterials. *Nat. Mater.* **11**, 936–941. (doi:10.1038/nmat3433)
101. Boyd DA *et al.* 2015 Single-step deposition of high-mobility graphene at reduced temperatures. *Nat. Commun.* **6**, 6620. (doi:10.1038/ncomms7620)
102. Efetov DK, Kim P. 2010 Controlling electron-phonon interactions in graphene at ultrahigh carrier densities. *Phys. Rev. Lett.* **105**, 256805. (doi:10.1103/PhysRevLett.105.256805)
103. Mak KF, Ju L, Wang F, Heinz TF. 2012 Optical spectroscopy of graphene: from the far infrared to the ultraviolet. *Solid State Commun.* **152**, 1341–1349. (doi:10.1016/j.ssc.2012.04.064)
104. Rouhi N, Capdevila S, Jain D, Zand K, Wang YY, Brown E, Jofre L, Burke P. 2012 Terahertz graphene optics. *Nano Research* **5**, 667–678. (doi:10.1007/s12274-012-0251-0)

105. Freitag M, Low T, Zhu W, Yan H, Xia F, Avouris P. 2013 Photocurrent in graphene harnessed by tunable intrinsic plasmons. *Nat. Commun.* **4**, 1951. (doi:10.1038/ncomms2951)
106. Rodrigo D, Limaj O, Janner D, Etezadi D, García De Abajo FJ, Pruneri V, Altug H. 2015 Mid-infrared plasmonic biosensing with graphene. *Science* **349**, 165–168. (doi:10.1126/science.aab2051)
107. Yang X *et al.* 2016 Far-field spectroscopy and near-field optical imaging of coupled plasmon-phonon polaritons in 2D van der Waals heterostructures. *Adv. Mater.* **28**, 2931–2938. (doi:10.1002/adma.201505765)
108. Fallah S, Rouhi K, Abdolali A. 2020 Optimized chemical potential graphene-based coding metasurface approach for dynamic manipulation of terahertz wavefront. *J. Phys. D: Appl. Phys.* **53**, 085102. (doi:10.1088/1361-6463/ab572f)
109. Hosseininejad SE, Rouhi K, Neshat M, Faraji-Dana R, Cabellos-Aparicio A, Abadal S, Alarcón E. 2019 Reprogrammable graphene-based metasurface mirror with adaptive focal point for THz imaging. *Sci. Rep.* **9**, 1–9. (doi:10.1038/s41598-019-39266-3)
110. Zhang Y, Feng Y, Zhao J, Jiang T, Zhu B. 2017 Terahertz beam switching by electrical control of graphene-enabled tunable metasurface. *Sci. Rep.* **7**, 14147. (doi:10.1038/s41598-017-14493-8)
111. Zeng B, Huang Z, Singh A, Yao Y, Azad AK, Mohite AD, Taylor AJ, Smith DR, Chen HT. 2018 Hybrid graphene metasurfaces for high-speed mid-infrared light modulation and single-pixel imaging. *Light: Sci. Appl.* **7**, 51. (doi:10.1038/s41377-018-0055-4)
112. Zeng F, Ye L, Li L, Wang Z, Zhao W, Zhang Y. 2019 Tunable mid-infrared dual-band and broadband cross-polarization converters based on U-shaped graphene metamaterials. *Opt. Express* **27**, 33826. (doi:10.1364/oe.27.033826)
113. Balci O, Kakenov N, Karademir E, Balci S, Cakmakyapan S, Polat EO, Caglayan H, Ozbay E, Kocabas C. 2018 Electrically switchable metadevices via graphene. *Sci. Adv.* **4**, eaao1749. (doi:10.1126/sciadv.aao1749)
114. Du W, Zhou Y, Yao Z, Huang Y, He C, Zhang L, He Y, Zhu L, Xu X. 2019 Active broadband terahertz wave impedance matching based on optically doped graphene-silicon heterojunction. *Nanotechnology* **30**, 195705. (doi:10.1088/1361-6528/ab0329)
115. Gao R-M, Xu Z-C, Ding C-F, Yao J-Q. 2016 Intensity-modulating graphene metamaterial for multiband terahertz absorption. *Appl. Opt.* **55**, 1929. (doi:10.1364/ao.55.001929)
116. Hosseininejad SE, Rouhi K, Neshat M, Cabellos-Aparicio A, Abadal S, Alarcon E. 2019 Digital metasurface based on graphene: an application to beam steering in terahertz plasmonic antennas. *IEEE Trans. Nanotechnol.* **18**, 734–746. (doi:10.1109/TNANO.2019.2923727)
117. Biswas SR, Gutiérrez CE, Nemilentsau A, Lee IH, Oh SH, Avouris P, Low T. 2018 Tunable graphene metasurface reflectarray for cloaking, illusion, and focusing. *Phys. Rev. Appl.* **9**, 034021. (doi:10.1103/PhysRevApplied.9.034021)
118. Yang Y, Lin H, Zhang BY, Zhang Y, Zheng X, Yu A, Hong M, Jia B. 2019 Graphene-based multilayered metamaterials with phototunable architecture for on-chip photonic devices. *ACS Photonics* **6**, 1033–1040. (doi:10.1021/acsphotonics.9b00060)
119. Lin H, Sturmberg BCP, Lin K-T, Yang Y, Zheng X, Chong TK, de Sterke CM, Jia B. 2019 A 90-nm-thick graphene metamaterial for strong and extremely broadband absorption of unpolarized light. *Nat. Photonics* **13**, 270–276. (doi:10.1038/s41566-019-0389-3)
120. Han S, Kim S, Kim S, Low T, Brar VW, Jang MS. 2020 Complete complex amplitude modulation with electronically tunable graphene plasmonic metamolecules. *ACS Nano* **14**, 1166–1175. (doi:10.1021/acsnano.9b09277)
121. Zheng W, Fan F, Chen M, Chen S, Chang SJ. 2016 Optically pumped terahertz wave modulation in MoS2-Si heterostructure metasurface. *AIP Adv.* **6**, 075105. (doi:10.1063/1.4958878)
122. Manzeli S, Ovchinnikov D, Pasquier D, Yazyev OV, Kis A. 2017 2D transition metal dichalcogenides. *Nat. Rev. Mater.* **2**, 17 033. (doi:10.1038/natrevmats.2017.33)
123. Chen S, Fan F, Miao Y, He X, Zhang K, Chang S. 2016 Ultrasensitive terahertz modulation by silicon-grown MoS2 nanosheets. *Nanoscale* **8**, 4713–4719. (doi:10.1039/c5nr08101g)
124. Mak KF, Lee C, Hone J, Shan J, Heinz TF. 2010 Atomically thin MoS2: a new direct-gap semiconductor. *Phys. Rev. Lett.* **105**, 136805. (doi:10.1103/PhysRevLett.105.136805)

125. Splendiani A, Sun L, Zhang Y, Li T, Kim J, Chim CY, Galli G, Wang F. 2010 Emerging photoluminescence in monolayer MoS2. *Nano Lett.* **10**, 1271–1275. (doi:10.1021/nl903868w)
126. Cheiwchanchamnangij T, Lambrecht WRL. 2012 Quasiparticle band structure calculation of monolayer, bilayer, and bulk MoS_2. *Phys. Rev. B Condens. Matter Mater. Phys.* **85**, 205302. (doi:10.1103/PhysRevB.85.205302)
127. Lopez-Sanchez O, Lembke D, Kayci M, Radenovic A, Kis A. 2013 Ultrasensitive photodetectors based on monolayer MoS_2. *Nat. Nanotechnol.* **8**, 497–501. (doi:10.1038/nnano.2013.100)
128. Cao Y, Gan S, Geng Z, Liu J, Yang Y, Bao Q, Chen H. 2016 Optically tuned terahertz modulator based on annealed multilayer MoS_2. *Sci. Rep.* **6**, 22899. (doi:10.1038/srep22899)
129. Lloyd-Hughes J, Jeon TI. 2012 A review of the terahertz conductivity of bulk and nano-materials. *J. Infrared, Millimeter, Terahertz Waves* **33**, 871–925. (doi:10.1007/s10762-012-9905-y)
130. Choudhury SM, Wang D, Chaudhuri K, Devault C, Kildishev A V., Boltasseva A, Shalaev VM. 2018 Material platforms for optical metasurfaces. *Nanophotonics* **7**, 959–987. (doi:10.1515/nanoph-2017-0130)
131. Liu H, Lu J, Wang XR. 2018 Metamaterials based on the phase transition of VO_2. *Nanotechnology* **29**, 024002. (doi:10.1088/1361-6528/aa9cb1)
132. Raeis-Hosseini N, Rho J. 2017 Metasurfaces based on phase-change material as a reconfigurable platform for multifunctional devices. *Materials* **10**, 1046. (doi:10.3390/ma10091046)
133. Rao CNR, Natarajan M, Subba Rao GV, Loehman RE. 1971 Phase transitions and conductivity anomalies in solid solutions of VO_2 with TiO_2, NbO_2, and MoO_2. *J. Phys. Chem. Solids* **32**, 1147–1150. (doi:10.1016/S0022-3697(71)80172-5)
134. Jung P, Ustinov A V., Anlage SM. 2014 Progress in superconducting metamaterials. *Supercond. Sci. Technol.* **27**, 073001. (doi:10.1088/0953-2048/27/7/073001)
135. Morin FJ. 1959 Oxides which show a metal-to-insulator transition at the Neel temperature. *Phys. Rev. Lett.* **3**, 34–36. (doi:10.1103/PhysRevLett.3.34)
136. Torrance JB, Lacorre P, Nazzal AI, Ansaldo EJ, Niedermayer C. 1992 Systematic study of insulator-metal transitions in perovskites RNiO3 (R=Pr,Nd,Sm,Eu) due to closing of charge-transfer gap. *Phys. Rev. B* **45**, 8209–8212. (doi:10.1103/PhysRevB.45.8209)
137. Hilton DJ, Prasankumar RP, Fourmaux S, Cavalleri A, Brassard D, El Khakani MA, Kieffer JC, Taylor AJ, Averitt RD. 2007 Enhanced photosusceptibility near Tc for the light-induced insulator-to-metal phase transition in vanadium dioxide. *Phys. Rev. Lett.* **99**, 226401. (doi:10.1103/PhysRevLett.99.226401)
138. Cavalleri A, Tóth C, Siders CW, Squier JA, Ráksi F, Forget P, Kieffer JC. 2001 Femtosecond structural dynamics in vo2 during an ultrafast solid-solid phase transition. *Phys. Rev. Lett.* **87**, 237401-1–237401-4. (doi:10.1103/PhysRevLett.87.237401)
139. Xiao Y *et al.* 2015 Ultrafast terahertz modulation characteristic of tungsten doped vanadium dioxide nanogranular film revealed by time-resolved terahertz spectroscopy. *Appl. Phys. Lett.* **107**, 031906. (doi:10.1063/1.4927383)
140. Jeong YG *et al.* 2015 A vanadium dioxide metamaterial disengaged from insulator-to-metal transition. *Nano Lett.* **15**, 6318–6323. (doi:10.1021/acs.nanolett.5b02361)
141. Zhang Y, Qiao S, Sun L, Shi QW, Huang W, Li L, Yang Z. 2014 Photoinduced active terahertz metamaterials with nanostructured vanadium dioxide film deposited by sol-gel method. *Opt. Express* **22**, 11070. (doi:10.1364/oe.22.011070)
142. Kübler C, Ehrke H, Huber R, Lopez R, Halabica A, Haglund RF, Leitenstorfer A. 2007 Coherent structural dynamics and electronic correlations during an ultrafast insulator-to-metal phase transition in VO_2. *Phys. Rev. Lett.* **99**, 116401. (doi:10.1103/PhysRevLett.99.116401)
143. Jeong J, Aetukuri N, Graf T, Schladt TD, Samant MG, Parkin SSP. 2013 Suppression of metal-insulator transition in VO2 by electric field-induced oxygen vacancy formation. *Science* **339**, 1402–1405. (doi:10.1126/science.1230512)
144. Shen Z, Zhou S, Ge S, Duan W, Chen P, Wang L, Hu W, Lu Y. 2018 Liquid-crystal-integrated metadevice: towards active multifunctional terahertz wave manipulations. *Opt. Lett.* **43**, 4695. (doi:10.1364/OL.43.004695)

145. Nouman MT, Hwang JH, Faiyaz M, Lee K-J, Noh D-Y, Jang J-H. 2018 Vanadium dioxide based frequency tunable metasurface filters for realizing reconfigurable terahertz optical phase and polarization control. *Opt. Express* **26**, 12922. (doi:10.1364/oe.26.012922)
146. Li C *et al.* 2016 Electrically tunable superconducting terahertz metamaterial with low insertion loss and high switchable ratios. *Appl. Phys. Lett.* **109**, 022601. (doi:10.1063/1.4955454)
147. Singh R, Xiong J, Azad AK, Yang H, Trugman SA, Jia QX, Taylor AJ, Chen H-T. 2012 Optical tuning and ultrafast dynamics of high-temperature superconducting terahertz metamaterials. *Nanophotonics* **1**, 117–123. (doi:10.1515/nanoph-2012-0007)
148. Anlage SM. 2011 The physics and applications of superconducting metamaterials. *J. Opt.* **13**, 024001. (doi:10.1088/2040-8978/13/2/024001)
149. Singh R, Xiong J, Roy Chowdhury D, Yang H, Azad AK, Trugman SA, Jia QX, Taylor AJ, Chen H-T. 2012 Thermal and ultrafast optical tuning of ultrathin high-temperature superconducting terahertz metamaterials. In *Metamaterials VII* (eds AD Boardman, NP Johnson, RW Ziolkowski), p. 84230Y.
150. Lagerwall JPF, Scalia G. 2012 A new era for liquid crystal research: applications of liquid crystals in soft matter nano-, bio- and microtechnology. *Curr. Appl. Phys.* **12**, 1387–1412. (doi:10.1016/j.cap.2012.03.019)
151. Shrekenhamer D, Chen W-C, Padilla WJ. 2013 Liquid crystal tunable metamaterial absorber. *Phys. Rev. Lett.* **110**, 177403. (doi:10.1103/PhysRevLett.110.177403)
152. Hokmabadi MP, Tareki A, Rivera E, Kung P, Lindquist RG, Kim SM. 2017 Investigation of tunable terahertz metamaterial perfect absorber with anisotropic dielectric liquid crystal. *AIP Adv.* **7**, 015102. (doi:10.1063/1.4973638)
153. Cui TJ, Liu S, Bai GD, Ma Q. 2019 Direct transmission of digital message via programmable coding metasurface. *Research* **2019**, 1–12. (doi:10.34133/2019/2584509)
154. Wan X, Zhang Q, Yi Chen T, Zhang L, Xu W, Huang H, Kun Xiao C, Xiao Q, Jun Cui T. 2019 Multichannel direct transmissions of near-field information. *Light: Sci. Appl.* **8**, 60. (doi:10.1038/s41377-019-0169-3)
155. Dai JY, Tang WK, Zhao J, Li X, Cheng Q, Ke JC, Chen MZ, Jin S, Cui TJ. 2019 Wireless communications through a simplified architecture based on time-domain digital coding metasurface. *Adv. Mater. Technol.* **4**, 1900044. (doi:10.1002/admt.201900044)
156. Tasolamprou AC *et al.* 2019 Exploration of intercell wireless millimeter-wave communication in the landscape of intelligent metasurfaces. *IEEE Access* **7**, 122 931–122 948. (doi:10.1109/ACCESS.2019.2933355)
157. Zhong S. 2019 Progress in terahertz nondestructive testing: a review. *Front. Mech. Eng.* **14**, 273–281. (doi:10.1007/s11465-018-0495-9)
158. Zhong S, Shen YC, Evans M, Zeitler JA, May RK, Gladden LF, Byers C. 2009 Quantification of thin-film coating thickness of pharmaceutical tablets using wavelet analysis of terahertz pulsed imaging data. In *34th Int. Conf. on Infrared, Millimeter, and Terahertz Waves, IRMMW-THz 2009, Busan, South Korea, 21–25 Sept. 2009*, pp. 1–2. IEEE.
159. Ryu CH, Park SH, Kim DH, Jhang KY, Kim HS. 2016 Nondestructive evaluation of hidden multi-delamination in a glass-fiber-reinforced plastic composite using terahertz spectroscopy. *Compos. Struct.* **156**, 338–347. (doi:10.1016/j.compstruct.2015.09.055)
160. Tu W, Zhong S, Incecik A, Fu X. 2018 Defect feature extraction of marine protective coatings by terahertz pulsed imaging. *Ocean Eng.* **155**, 382–391. (doi:10.1016/j.oceaneng.2018.01.033)
161. Wang L, Li L, Li Y, Zhang HC, Cui TJ. 2016 Single-shot and single-sensor high/super-resolution microwave imaging based on metasurface. *Sci. Rep.* **6**, 26959. (doi:10.1038/srep26959)
162. Li YB, Li LL, Xu BB, Wu W, Wu RY, Wan X, Cheng Q, Cui TJ. 2016 Transmission-type 2-bit programmable metasurface for single-sensor and single-frequency microwave imaging. *Sci. Rep.* **6**, 23731. (doi:10.1038/srep23731)
163. Li L, Ruan H, Liu C, Li Y, Shuang Y, Alù A, Qiu CW, Cui TJ. 2019 Machine-learning reprogrammable metasurface imager. *Nat. Commun.* **10**, 1082. (doi:10.1038/s41467-019-09103-2)
164. Johnson JL, Dorney TD, Mittleman DM. 2001 Enhanced depth resolution in terahertz imaging using phase-shift interferometry. *Appl. Phys. Lett.* **78**, 835–837. (doi:10.1063/1.1346626)

165. Chan WL, Moravec ML, Baraniuk RG, Mittleman DM. 2007 Terahertz imaging with compressed sensing and phase retrieval. *Optics InfoBase Conference Papers* **33**, 974–976. (doi:10.1364/ol.33.000974)
166. Hunt J, Driscoll T, Mrozack A, Lipworth G, Reynolds M, Brady D, Smith DR. 2013 Metamaterial apertures for computational imaging. *Science* **339**, 310–313. (doi:10.1126/science.1230054)
167. Chen WT, Zhu AY, Sanjeev V, Khorasaninejad M, Shi Z, Lee E, Capasso F. 2018 A broadband achromatic metalens for focusing and imaging in the visible. *Nat. Nanotechnol.* **13**, 220–226. (doi:10.1038/s41565-017-0034-6)
168. Jiang X *et al.* 2018 All-dielectric metalens for terahertz wave imaging. *Opt. Express* **26**, 14132. (doi:10.1364/oe.26.014132)
169. Zang XF *et al.* 2020 Polarization-insensitive metalens with extended focal depth and longitudinal high-tolerance imaging. *Adv. Opt. Mater.* **8**, 1–9. (doi:10.1002/adom.201901342)
170. Sleasman T, F. Imani M, Gollub JN, Smith DR. 2015 Dynamic metamaterial aperture for microwave imaging. *Appl. Phys. Lett.* **107**, 204104. (doi:10.1063/1.4935941)
171. Sleasman T, Boyarsky M, Imani MF, Fromenteze T, Gollub JN, Smith DR. 2017 Single-frequency microwave imaging with dynamic metasurface apertures. *J. Opt. Soc. Am. B* **34**, 1713. (doi:10.1364/josab.34.001713)
172. Li L *et al.* 2019 Intelligent metasurface imager and recognizer. *Light: Sci. Appl.* **8**, 1–9. (doi:10.1038/s41377-019-0209-z)
173. Xie L, Gao W, Shu J, Ying Y, Kono J. 2015 Extraordinary sensitivity enhancement by metasurfaces in terahertz detection of antibiotics. *Sci. Rep.* **5**, 1–4. (doi:10.1038/srep08671)
174. Bui TS, Dao TD, Dang LH, Vu LD, Ohi A, Nabatame T, Lee Y, Nagao T, Hoang CV. 2016 Metamaterial-enhanced vibrational absorption spectroscopy for the detection of protein molecules. *Sci. Rep.* **6**, 1–7. (doi:10.1038/srep32123)
175. Wallace VP, Fitzgerald AJ, Pickwell E, Pye RJ, Taday PF, Flanagan N, Thomas HA. 2006 Terahertz pulsed spectroscopy of human basal cell carcinoma. *Appl. Spectrosc.* **60**, 1127–1133. (doi:10.1366/000370206778664635)
176. Woodward RM, Wallace VP, Pye RJ, Cole BE, Arnone DD, Linfield EH, Pepper M. 2003 Terahertz pulse imaging of ex vivo basal cell carcinoma. *J. Invest. Dermatol.* **120**, 72–78. (doi:10.1046/j.1523-1747.2003.12013.x)
177. Lee DK *et al.* 2015 Highly sensitive and selective sugar detection by terahertz nano-antennas. *Sci. Rep.* **5**, 1–7. (doi:10.1038/srep15459)
178. Yang Y, Xu D, Zhang W. 2018 High-sensitivity and label-free identification of a transgenic genome using a terahertz meta-biosensor. *Opt. Express* **26**, 31589. (doi:10.1364/oe.26.031589)
179. Park SJ, Son BH, Choi SJ, Kim HS, Ahn YH. 2014 Sensitive detection of yeast using terahertz slot antennas. *Opt. Express* **22**, 30467. (doi:10.1364/oe.22.030467)
180. Park SJ *et al.* 2014 Detection of microorganisms using terahertz metamaterials. *Sci. Rep.* **4**, 4988. (doi:10.1038/srep04988)
181. O'Hara JF, Withayachumnankul W, Al-Naib I. 2012 A review on thin-film sensing with terahertz waves. *J. Infrared, Millimeter Terahertz Waves* **33**, 245–291. (doi:10.1007/s10762-012-9878-x)
182. Brolo AG, Gordon R, Leathem B, Kavanagh KL. 2004 Surface plasmon sensor based on the enhanced light transmission through arrays of nanoholes in gold films. *Langmuir* **20**, 4813–4815. (doi:10.1021/la0493621)
183. Deng X, Li L, Enomoto M, Kawano Y. 2019 Continuously frequency-tuneable plasmonic structures for terahertz bio-sensing and spectroscopy. *Sci. Rep.* **9**, 1–9. (doi:10.1038/s41598-019-39015-6)
184. Park SJ, Cha SH, Shin GA, Ahn YH. 2017 Sensing viruses using terahertz nano-gap metamaterials. *Biomed. Opt. Exp.* **8**, 3551. (doi:10.1364/boe.8.003551)
185. Yang P, Xiao Y, Xiao M, Li S. 2019 6G wireless communications: vision and potential techniques. *IEEE Network* **33**, 70–75. (doi:10.1109/MNET.2019.1800418)
186. Lee YS. 2009 *Principles of terahertz science and technology*. Boston, MA: Springer US.
187. Grimberg R, Tian GY. 2012 High-frequency electromagnetic non-destructive evaluation for high spatial resolution, using metamaterials. *Proc. R. Soc. A* **468**, 3080–3099. (doi:10.1098/rspa.2011.0666)